



1

2 **Regional CO₂ Fluxes during 2010-2015 Inferred from GOSAT XCO₂**
3 **retrievals using a new version of Global Carbon Assimilation System**

4

5 Fei Jiang^{1,7*}, Hengmao Wang¹, Jing M. Chen², Weimin Ju¹, Xiangjun Tian³, Shuzhang
6 Feng¹, Guicai Li⁴, Zhuoqi Chen⁵, Shupeng Zhang⁵, Xuehe Lu¹, Jane Liu^{2,6}, Haikun
7 Wang⁶, Jun Wang¹, Wei He¹, Mousong Wu¹

8

9

10 *1 Jiangsu Provincial Key Laboratory of Geographic Information Science and Technology,*
11 *International Institute for Earth System Science, Nanjing University, Nanjing, 210023, China*

12 *2 Department of Geography and Planning, University of Toronto, Toronto, Ontario M5S3G3,*
13 *Canada*

14 *3 The Institute of Atmospheric Physics, Chinese Academy of Sciences, Beijing, 100029, China*

15 *4 National Satellite Meteorological Center, China Meteorological Administration, Beijing*
16 *100101, China*

17 *5 College of Global Change and Earth System Science, Beijing Normal University, Beijing,*
18 *100875, China*

19 *6 School of Atmospheric Sciences, Nanjing University, Nanjing, 210023, China*

20 *7 Jiangsu Center for Collaborative Innovation in Geographical Information Resource*
21 *Development and Application, Nanjing, 210023, China*

22

23

24

25

26

* Corresponding author: Tel.: +86-25-83597077; Fax: +86-25-83592288; E-mail address: jiangf@nju.edu.cn



27 **Abstract**

28 Satellite XCO₂ retrievals could help to improve carbon flux estimation because of
29 their good spatial coverage. In this study, to assimilate the GOSAT XCO₂ retrievals,
30 the Global Carbon Assimilation System (GCAS) is upgraded with new assimilation
31 algorithms, procedures and a localization scheme, a higher assimilation parameter
32 resolution and so on, and hence is named as GCASv2. Based on this new system, the
33 global terrestrial ecosystem (BIO) and ocean (OCN) carbon fluxes from May 1, 2009
34 to Dec 31, 2015 are constrained using the GOSAT ACOS XCO₂ retrievals (Version 7.3).
35 The posterior carbon fluxes from 2010 to 2015 are independently evaluated using CO₂
36 observations from 52 surface flask sites. The results show that the posterior carbon
37 fluxes could significantly improve the modeling of atmospheric CO₂ concentrations,
38 with global mean BIAS decreases from a prior value of 1.6±1.8 ppm to -0.5±1.8 ppm.
39 Globally, the mean annual BIO and OCN carbon sinks and their interannual variations
40 inferred in this study are very close to the estimates of CT2017 during the study period,
41 and the inferred mean atmospheric CO₂ growth rate and its interannual changes are also
42 very close to the observations. Regionally, over the northern lands, there are the
43 strongest carbon sinks in North America Temperate, followed by Europe, Boreal Asia,
44 and Temperate Asia; and in tropics, there are strong sinks in Tropical South America
45 and Tropical Asia, but a very weak sink in Africa. This pattern is significantly different
46 from the estimates of CT2017, but the estimated carbon sinks in each continent and
47 some key regions like Boreal Asia and Amazon are comparable or in the range of
48 previous bottom-up estimates. The inversion also changes the interannual variations of
49 carbon fluxes in most TRANSCOM land regions, which have a better relationship with
50 the changes of severe drought area or LAI, or are more consistent with previous
51 estimates for the impact of drought. These results suggest that the GCASv2 system
52 works well with the GOSAT XCO₂ retrievals, and has a good performance in estimating
53 the surface carbon fluxes, meanwhile, our results also indicate that the GOSAT XCO₂
54 retrievals could help to better understand the interannual variations of regional carbon
55 fluxes.



56 **1. Introduction**

57 Atmospheric carbon dioxide (CO₂) is one of the most important greenhouse gases,
58 and fossil fuel burning and land use change are mostly responsible for its increase from
59 the preindustrial concentration. Terrestrial ecosystems and oceans play very important
60 roles in regulating the atmospheric CO₂ concentration. In the past half century, about
61 60% of the anthropogenic CO₂ emissions have been absorbed by the terrestrial
62 ecosystems and oceans (IPCC, 2014). However, their carbon uptakes have significant
63 spatial differences and inter-annual variations. Therefore, it is very important to
64 quantify the global and regional carbon fluxes.

65 Atmospheric inversion is an effective method for estimating the surface CO₂ fluxes
66 using the globally distributed atmospheric CO₂ concentration observations (Enting and
67 Newsam, 1990; Gurney et al., 2002). It has robust performance on global or hemisphere
68 scale carbon budget estimates (Houweling et al., 2015), but on regional scales, due to
69 the uneven distribution of in situ observations, the reliability of inversion results varies
70 greatly in different regions. Generally, the inversions have large uncertainties in tropics,
71 southern hemisphere oceans and most continental interiors such as South America,
72 Africa, and Boreal Asia (Peylin et al., 2013). Satellite observation has a better spatial
73 coverage, especially over remote regions, and studies show that it can be used to
74 improve the carbon flux estimates (e.g., Chevallier et al., 2007; Miller et al., 2007;
75 Hungershofer et al., 2010). The Greenhouse Gases Observing Satellite (GOSAT)
76 (Kuze et al., 2009), being the first satellite mission dedicated to observing CO₂ from
77 space, was launched in 2009. Many inversions have utilized the GOSAT retrievals for
78 column-averaged dry air mole fractions of CO₂ (XCO₂) to infer surface carbon fluxes
79 (e.g., Basu et al., 2013; Maksyutov et al., 2013; Saeki et al., 2013a; Chevallier et al.,
80 2014; Deng et al., 2014; Deng et al., 2016; Wang et al., 2018; Wang et al., 2019). Takagi
81 et al. (2011) found that GOSAT XCO₂ retrievals could significantly reduce the
82 uncertainties in estimates of surface CO₂ fluxes for regions in Africa, South America,
83 and Asia, where the sparsity of the surface monitoring sites is most evident. Basu et al.
84 (2013) shown that assimilating only GOSAT data can well reproduce the observed CO₂



85 time series at the surface and TCCON sites in the tropics and the northern extra-tropics,
86 but enhance seasonal cycle amplitudes in the southern extra-tropics. Wang et al. (2019)
87 also showed that GOSAT XCO₂ retrievals can effectively improve carbon flux
88 estimation, and the performance of the inversion with GOSAT data only was
89 comparable with the one using in situ observations. Meanwhile, based on the inversions
90 with GOSAT XCO₂ retrievals, Liu et al. (2018) quantified the impacts of the 2011 and
91 2012 droughts on terrestrial ecosystem carbon uptake anomalies over the contiguous
92 US, Deng et al. (2016) compared the distributions of drought and posterior carbon
93 fluxes in South America for 2010-2012, Detmers et al. (2015) studied the impact of the
94 strong La Niña episode on the carbon fluxes in Australia from the end of 2010 to early
95 2012. However, so far, on the one hand, most studies focused on the impact of GOSAT
96 XCO₂ retrievals on the inversion of surface carbon fluxes, but in many regions, there
97 are still large divergences for carbon sinks between different inversions with the same
98 GOSAT data or between inversions with GOSAT and in situ observations (Chevallier
99 et al., 2014), on the other hand, although some studies reported the impact of drought
100 or extreme wetness on the changes of carbon fluxes using inversions based on GOSAT,
101 few studies have comprehensively investigated the impacts of GOSAT data on the
102 interannual variations of inverted land sinks in different regions.

103 In this study, we present a 6-year inversion from 2010 to 2015 for the global and
104 regional carbon fluxes using only the GOSAT XCO₂ retrievals. The Global Carbon
105 Assimilation System (GCAS) is employed to conduct this inversion, which was
106 developed in China in 2015 (Zhang et al., 2015) and updated in this study with a new
107 scheme to assimilate XCO₂ retrievals. The inverted multi-year averaged carbon fluxes
108 for the globe, global land and ocean, each TRANSCOM region as well as some key
109 areas are shown and compared with previous top-down and bottom-up (Jiang et al.,
110 2016) estimates. The estimated interannual variations of carbon fluxes in each
111 TRANSCOM region are given and discussed against changes in drought and LAI. This
112 manuscript is organized as follows: Section 2 details the GCASv2 system as well as the
113 prior fluxes, GOSAT retrievals and uncertainty settings. Section 3 briefly introduces the



114 experimental design. Results and discussions are presented in Section 4, and
115 Conclusions are given in Section 5.

116 **2. Method and Data**

117 **2.1 A new version of the Global Carbon Assimilation System (GCASv2)**

118 Figure 1 shows the flow chart of the GCASv2 system. In each data assimilation
119 (DA) window, there are two steps. The first step, the prior fluxes of X^b are perturbed
120 with a Gaussian random distribution, and put into the global atmospheric chemical
121 transport model MOZART-4 to simulate CO₂ concentrations, which are then sampled
122 according to the locations and times of CO₂ observations. The sampled data are used in
123 the assimilation module together with the CO₂ observations to generate the optimized
124 fluxes of X^a . In the second step, the MOZART-4 model is run again using the
125 optimized fluxes of X^a , to generate new CO₂ concentrations for the initial field of the
126 next DA window. This DA flow chart is different from the previous version of GCAS,
127 which runs the MOZART-4 model only once, and optimizes the fluxes and the initial
128 field of the next window synchronously. In this study, we find the synchronous dual
129 optimizations will weaken the assimilation benefits on fluxes.

130 The perturbation of X^b represents the uncertainty of the prior carbon flux, which
131 is calculated using the following function.

$$132 \quad X_i^b = X_0^b + \lambda \times \delta_i \times X_0^b, \quad i = 1, 2, \dots, N \quad (1)$$

133 where δ_i represents random perturbation samples, which is drawn from Gaussian
134 distributions with mean zero and standard deviation of one. N is the ensemble size. λ is
135 a set of scaling factors, which represents the uncertainty of each prior flux. In previous
136 version GCAS, λ is defined in different land and ocean areas based on 22 TRANSCOM
137 regions (Gurney et al., 2002) and 19 Olson ecosystem types, as in CarbonTracker
138 (Peters et al., 2007). This means that in the same area, the error of a prior flux is the
139 same. Through assimilation, the flux will be integrally enlarged or reduced. In GCASv2,
140 we change to use a λ in each grid, meaning that for each grid, the perturbations of prior
141 fluxes are independent. In addition, the grid cell of λ is different from those of the prior
142 flux and the transport model, which could be set freely.



143 Generally, there are 4 types of carbon fluxes, namely terrestrial ecosystem (BIO)
144 carbon flux, atmosphere and ocean (OCN) carbon exchange, fossil fuel (FOSSIL)
145 carbon emission and biomass burning (FIRE) carbon emission, which are used to drive
146 the transport model to simulate the atmospheric CO₂ concentration. And in general,
147 FOSSIL and FIRE fluxes are assumed to have no errors, only BIO and OCN fluxes are
148 optimized in an assimilation system (e.g., Peters, et al., 2007; Jiang et al., 2013; Wang
149 et al., 2019). In GCASv1, only the BIO flux was optimized, the OCN flux was directly
150 from the output of CarbonTraker (CT). In GCASv2, it is set to be an optional item. Four
151 schemes are set (Functions 2 - 5). The first one is the same as the previous version, only
152 the BIO flux is optimized; the second one is the same as general, namely both BIO and
153 OCN fluxes are optimized; the third one is that BIO, OCN and FOSSIL fluxes are
154 optimized at the same time; and the fourth one is that only net flux is optimized.

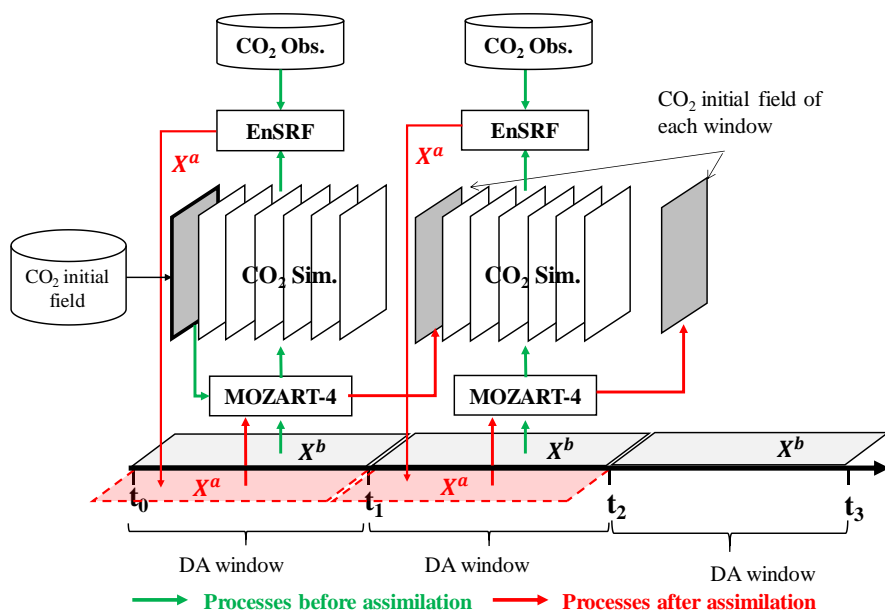
$$155 \quad X_i^b = (X_{bio}^b + \lambda_{bio} \times \delta_{i,bio} \times X_{bio}^b) + X_{ocn}^b + X_{fossil}^b + X_{fire}^b, i = 1, 2, \dots, N \quad (2)$$

$$156 \quad X_i^b = (X_{bio}^b + \lambda_{bio} \times \delta_{i,bio} \times X_{bio}^b) + (X_{ocn}^b + \lambda_{ocn} \times \delta_{i,ocn} \times X_{ocn}^b) \\ 157 \quad + X_{fossil}^b + X_{fire}^b, i = 1, 2, \dots, N \quad (3)$$

$$158 \quad X_i^b = (X_{bio}^b + \lambda_{bio} \times \delta_{i,bio} \times X_{bio}^b) + (X_{ocn}^b + \lambda_{ocn} \times \delta_{i,ocn} \times X_{ocn}^b) \\ 159 \quad + (X_{fossil}^b + \lambda_{fossil} \times \delta_{i,fossil} \times X_{fossil}^b) + X_{fire}^b, i = 1, 2, \dots, N \quad (4)$$

$$160 \quad X_i^b = (X_{bio}^b + X_{ocn}^b + X_{fossil}^b + X_{fire}^b) + \lambda_{netflux} \times \delta_{i,netflux} \times (X_{bio}^b + \\ 161 \quad X_{ocn}^b + X_{fossil}^b + X_{fire}^b), i = 1, 2, \dots, N \quad (5)$$

162



163

164

Figure 1. Flow chart of the GCASv2 system

165 2.1.1 EnSRF assimilation algorithm

166 To avoid storing and inverting very large matrices during analysis, the Ensemble
 167 square root filter (EnSRF) algorithm, introduced by Whitaker and Hamill (2002), is
 168 used to constrain the carbon fluxes in this version. EnSRF obviates the need to perturb
 169 the observations in contrast to the traditional EnKF algorithm and assimilates
 170 observations in a sequential way. It has a better performance than the method to
 171 assimilate observations simultaneously as long as the observation errors are
 172 uncorrelated (Houtekamer and Mitchell, 2001). The implementation process and setup
 173 are detailed below.

174 After obtaining an ensemble of state vectors as described in Section 2.1, ensemble
 175 runs of MOZART-4 are conducted to propagate these errors in the model with each
 176 ensemble sample of a state vector. The background error covariance P^b is calculated
 177 based on the forecast ensemble from Eq. (6):

178
$$P^b = \frac{1}{n-1} \sum_{i=1}^n (X_i^b - \bar{X}^b) (X_i^b - \bar{X}^b)^T \quad (6)$$



179 where $\bar{\mathbf{X}}^b$ represents the mean of the ensemble samples. Based on the background
180 error covariance, the response of the uncertainty in the simulated concentrations to the
181 uncertainty in emissions is obtained. Combining observational vector \mathbf{y} , the state vector
182 is updated according to the following formulations:

$$183 \quad \bar{\mathbf{X}}^a = \bar{\mathbf{X}}^b + \mathbf{K}(\mathbf{y} - \mathbf{H}\bar{\mathbf{X}}^b) \quad (7)$$

$$184 \quad \mathbf{K} = \mathbf{P}^b \mathbf{H}^T (\mathbf{H} \mathbf{P}^b \mathbf{H}^T + \mathbf{R})^{-1} \quad (8)$$

$$185 \quad \delta \mathbf{X}_i^a = \delta \mathbf{X}_i^b - \tilde{\mathbf{K}} \mathbf{H} \delta \mathbf{X}_i^b \quad (9)$$

186 While employing sequential assimilation and independent observations

$$187 \quad \tilde{\mathbf{K}} = (1 + \sqrt{\mathbf{R} / (\mathbf{H} \mathbf{P}^b \mathbf{H}^T + \mathbf{R})})^{-1} \mathbf{K} \quad (10)$$

188 where \mathbf{H} is the observation operator that maps the state variable from model space to
189 observation space. \mathbf{K} is the Kalman gain matrix of ensemble mean depending on
190 background and observation error covariance \mathbf{R} , representing the relative contributions
191 to analysis. $\tilde{\mathbf{K}}$ is the Kalman gain matrix of ensemble perturbation, and then emission
192 perturbations after inversion $\delta \mathbf{X}_i^a$ can be calculated. At the analysis step, the ensemble
193 mean $\bar{\mathbf{X}}^a$ is taken as the best estimate of the carbon flux.

194 To reduce the computational cost and the influence of representative errors, a
195 ‘super-observation’ approach is adopted based on the optimal estimation theory
196 (Miyazaki et al., 2012). A super-observation is generated by averaging all observations
197 located within the same model grid within a DA window. We assume that the
198 observation errors of different stations at different times are independent of each other.
199 The standard deviation of the j th observation y_j is r_j . The super-observation y_{new} ,
200 standard deviation r_{new} and corresponding simulations $x_{new,i}$ from one perturbed
201 prior flux X_i^b are calculated:

$$202 \quad 1/r_{new}^2 = \sum_{j=1}^m 1/r_j^2 \quad (7)$$



$$203 \quad y_{new} = \frac{\sum_{j=1}^m w_j y_j}{\sum_{j=1}^m w_j} \quad (8)$$

$$204 \quad x_{new,i} = \frac{\sum_{j=1}^m w_j x_{j,i}}{\sum_{j=1}^m w_j} \quad (9)$$

205 where $w_j = 1/r_j^2$ is the weighting factor; m is the number of observations within a
206 super-observation grid. The super-observation error decreases as the number of
207 observations used for the super-observation increases.

208 **2.1.2 Atmospheric transport model**

209 Same as the GCAS system (Zhang et al., 2015), the global chemical transport
210 Model for OZone And Related chemical Tracers (MOZART-4; Emmons et al., 2010) is
211 adopted as the atmospheric transport model in GCASv2. MOZART-4 is a flexible
212 model, it can be run at essentially any resolution, and can be driven by essentially any
213 meteorological data set and with any emission inventories (Emmons et al., 2010). In
214 this system, we preset two horizontal resolutions for MOZART runs, one being
215 approximately $2.8^\circ \times 2.8^\circ$, with model grids of 128×64 , and another being
216 approximately $1.0^\circ \times 1.0^\circ$, with model grids of 360×180 . In the vertical direction, we
217 use 28 layers. The ERA-Interim reanalysis datasets from the European Centre for
218 Medium-Range Weather Forecasts (ECMWF) are used to drive the model. ERA-
219 Interim data set includes as many as 128 meteorological variables, and has the highest
220 spatial resolution of approximately 80 km (T255 spectral) on 60 vertical levels from
221 the surface up to 0.1 hPa. Only the variables required for MOZART-4 with a spatial
222 resolution of $1.0^\circ \times 1.0^\circ$, and 28 vertical levels for 3-D variables from the surface to
223 approximately 2.5 hPa are selected in this system. The selected variables and vertical
224 levels are shown in Table S1 and S2 in the supporting information.

225 **2.1.3 DA window and localization**

226 The DA window is set to one week in GCASv2, which is the same as before.
227 Theoretically, a longer DA window is better, because CO_2 is a stable species. The longer
228 window, the farther CO_2 will be transported. In this way, more observation stations will
229 sense the flux change of one area, and thus more observations can be used to optimize



230 the flux of that place. However, the farther away, the weaker signal the stations can
231 sense. Limited by the method of EnKF, this weak signal will be masked by the method's
232 own unphysical signal (spurious correlation). In addition, Zhang et al. (2015) tested
233 different DA window lengths and found that the longer the window, the larger optimized
234 terrestrial carbon sink will be, resulting in a smaller optimized annual atmospheric CO₂
235 growth rate as compared to the observed rate. Therefore, they pointed out that the 1-
236 week DA window seems to be most suitable. For this reason, this study also uses the
237 same DA window of one week as before.

238 In the EnKF method, there are inevitably spurious correlations. Therefore, a
239 localization scale, which determines that only measurements located within a certain
240 distance (cutoff radius) from a grid point will influence the analysis of this grid, must
241 be set to reduce the effect of spurious correlations. The localization technique in this
242 study is based on both the distance between one site and one grid cell of λ , and the
243 linear correlation coefficient between the simulated concentrations and the perturbed
244 fluxes for each parameter (λ)/observation pair. If the distance is less than 500 km and
245 the correlation coefficient is greater than zero, the observations will be accepted for
246 assimilation, and if the distance is greater than/equal to 500 km and less than 3000 km
247 and the relationship between a parameter deviation and its modeled observational
248 impact is statistically significant ($p < 0.05$), then that relationship is retained. Otherwise,
249 the relationship is assumed to be spurious noise. The scale of 3000 km is set simply
250 according to the globally-averaged 80-m wind speed during the day (4.96 m/s, Archer
251 and Jacobson, 2005) and the length of DA window (1 week).

252 **2.2 Prior carbon fluxes**

253 As described in Section 2.1, there are 4 types of prior carbon fluxes in GCASv2.
254 In this study, FOSSIL carbon emissions are obtained from NOAA's CarbonTracker,
255 version CT2017 (Peters et al. 2007, with updates documented at
256 <http://carbontracker.noaa.gov>), which is an average of the Carbon Dioxide Information
257 Analysis Center (CDIAC) product (Andres et al., 2011) and the Open-source Data
258 Inventory of Anthropogenic CO₂ (ODIAC) emission product (Oda and Maksyutov,



259 2011). The FIRE CO₂ emissions are also taken from CT2017, which are the average of
260 the Global Fire Emissions Database version 4.1 (GFEDv4) (van der Werf et al., 2010;
261 Giglio et al., 2013) and the Global Fire Emission Database from the NASA Carbon
262 Monitoring System (GFED_CMS). The OCN CO₂ exchange is from the pCO₂-Clim
263 prior of CT2017, which is derived from the Takahashi et al. (2009) climatology of
264 seawater pCO₂. In addition, as shown in Figure 7 of the CarbonTracker Documentation
265 CT2017 release (<https://www.esrl.noaa.gov/gmd/ccgg/carbontracker/CT2017/>,
266 accessed on 4 Mar, 2020), there are no data in many seas like Japan Sea, Mediterranean,
267 Gulf of Mexico, East China Sea, and so on, and therefore, the fluxes in 2009 modeled
268 using the global ocean circulation (OPA) and the biogeochemistry model (PISCES-T)
269 (Buitenhuis et al., 2006; Jiang et al., 2013) is used to fill the no data areas.

270 The BIO carbon flux, which is the most important prior carbon flux in an
271 assimilation system, was simulated using the Boreal Ecosystems Productivity
272 Simulator (BEPS) model (Chen et al., 1999; Ju et al., 2006) in this study. BEPS is a
273 process-based, remote sensing data driven, and mechanistic ecosystem model. In this
274 study, BEPS model was run starting from 2000. To simplify the initialization, the initial
275 values of the different carbon pools are from a previous BEPS simulation (Chen et al.,
276 2019). In short, all carbon pools were assumed to be in a state of dynamic equilibrium
277 from 1901 to 1910. And all carbon pools were determined by solving a set of equations
278 describing the dynamics of carbon pools (Chen et al., 2003). Then the simulation
279 forwarded using historical data. Due to the lack of historical data of remote sensed LAI
280 data, the averaged LAI from 1982 to 1986 represented that over the 1901-1981 period.
281 Then, all our initial carbon pools were set to states of carbon pools in 2000 according
282 to Chen et al. (2019). The BEPS model was also driven by the 1°×1° ERA-Interim
283 reanalysis datasets, including relative humidity, wind speed, air temperature, incoming
284 solar radiation, and total precipitation. The other data include LAI data and clumping
285 index. LAI was inverted from surface reflectance datasets of Moderate Resolution
286 Imaging Spectroradiometer (MODIS) (Liu et al., 2012), and the clumping index was
287 derived from the MODIS Bidirectional Reflectance Distribution Function (BRDF)



288 products, which provided the finest pseudo multi-angular data for the land surface,
289 according to Normalized Difference between Hotspot and Darkspot (NDHD) (Chen et
290 al., 2005, He et al., 2012).

291 **2.3 GOSAT XCO₂ retrievals**

292 The GOSAT XCO₂ retrievals of the ACOS Version 7.3 Level 2 Lite product
293 (O'Dell et al., 2012; Crisp et al., 2012) at the pixel level during May 2009 ~ Dec 2015
294 is used in this study, which is bias-corrected (Wunch et al., 2011). In order to achieve
295 the most extensive spatial coverage with the assurance of using best quality data
296 available, before being used in the inversion system, the XCO₂ retrievals are filtered
297 with two parameters of warn_levels and xco2_quality_flag, which are provided along
298 with the product. Only the data with xco2_quality_flag greater than 0 are selected. The
299 selected data are then divided into three groups according the value of warn_levels, that
300 are with warn_levels less than 8, greater than 9 and less than 12, and greater than 13,
301 respectively. The group with smallest warn_levels has the best data quality, while that
302 with the largest is the worst. Then, the pixel data are averaged within the grid cell of
303 1°×1°, and in each grid, only the group with best data quality is selected and then
304 averaged. The other variables like column-averaging kernel, retrieval error and so on
305 which are provided along with the XCO₂ product are also dealt with the same method.
306 This process is the same as Wang et al. (2019).

307 For the modeled XCO₂, the simulated CO₂ concentration profile should be first
308 mapped into the satellite retrieval levels and then vertically integrated according to the
309 following equation.

$$310 \quad XCO_2^m = XCO_2^a + \sum_j h_j a_j (A(x) - y_{a,j}) \quad (10)$$

311 where j denotes the retrieval level; x is the simulated CO₂ profile, and $A(x)$ is a mapping
312 matrix; XCO_2^a is the prior XCO₂; h_j is a pressure weighting function, a_j and y_a are the
313 satellite column averaging kernel and the prior CO₂ profile for retrieval, respectively.
314 Except the simulated CO₂ profile, the other quantities are provided along with the
315 ACOS product and filtered and averaged to 1°×1° grid according to the above method.



316 2.4 Evaluation data and method

317 Generally, direct validation of the optimized flux is impossible, and instead, we
318 indirectly evaluate the posterior flux by comparing the forward simulated atmospheric
319 CO₂ mixing ratios against measurements (e.g., Jin et al., 2018; Wang et al., 2019; Feng
320 et al., 2020). First, the simulated XCO₂ are compared against the corresponding GOSAT
321 XCO₂ retrievals to test the effectiveness of the assimilation system (see Section 2.3 for
322 the description of the GOSAT XCO₂ retrieval). Second, Surface CO₂ observations used
323 for independent evaluations in this study are obtained from the
324 obspack_co2_1_GLOBALVIEWplus_v5.0_2019-08-12 product. It is a subset of the
325 Observation Package (ObsPack) Data Product (ObsPack, 2019), and contains a
326 collection of discrete and quasi-continuous measurements at surface, tower and ship
327 sites contributed by national and universities laboratories around the world. In this study,
328 surface CO₂ measurements from 52 flask sites are selected to evaluate the posterior CO₂
329 concentrations, which are all provided by the NOAA Global Monitoring Laboratory
330 (with lab number of 1 in each filename). The locations of the 52 sites could be found in
331 Figure 2 and the corresponding sites code as well as the information latitude and
332 longitude are listed in Table S3 in the Supporting Information.

333 During the evaluation, 3 basic statistical measures, namely mean bias (BIAS), root
334 mean square error (RMSE), and correlation coefficient (CORR), are calculated against
335 the surface CO₂ observations and GOSAT XCO₂ retrievals, respectively. The BIAS,
336 RMSE, and CORR reflect the overall model tendency, both the model bias and error
337 variance, and the linear correspondence between the modeled and observational
338 values/retrievals, respectively. The functions of these 3 basic statistical measures are
339 expressed as:

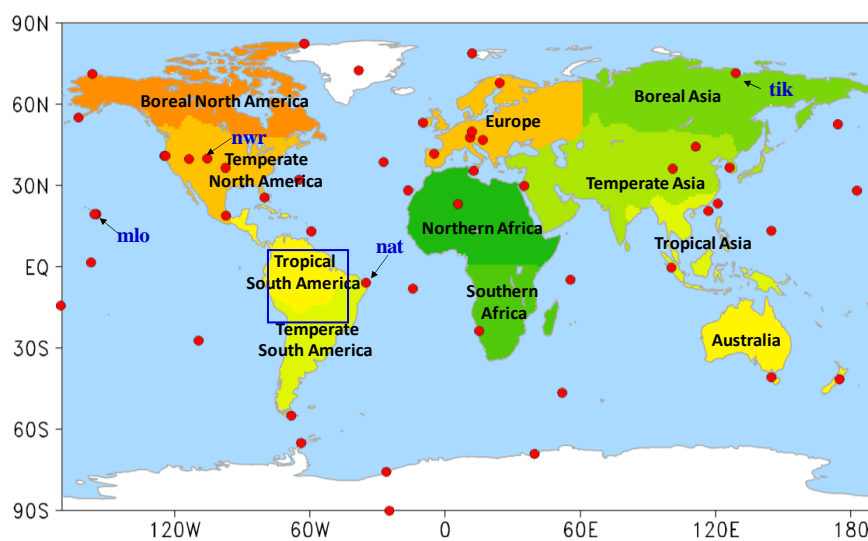
$$340 \quad BIAS = \frac{1}{M} \sum_{j=1}^M (x_j - y_j) = \bar{y} - \bar{x} \quad (10)$$

$$341 \quad RMSE = \sqrt{\frac{1}{M} \sum_{j=1}^M (x_j - y_j)^2} \quad (11)$$



$$CORR = \frac{\sum_{j=1}^M (x_j - \bar{x})(y_j - \bar{y})}{\sqrt{\sum_{j=1}^M (x_j - \bar{x})^2} \sqrt{\sum_{j=1}^M (y_j - \bar{y})^2}} \quad (12)$$

343 where x_j and y_j denote the modeled and the observational values/retrievals,
344 respectively, at the j th out of M records, and the overbars denote averages.



345
346 **Figure 2.** Distributions of the observation sites used in this study. Red solid circles are
347 the 52 surface flask sites used for evaluations, the shaded shows the 11 TRANSCOM
348 regions, the blue rectangle shows the Amazon region, which is defined the same as
349 Botta et al. (2012)

350 3. Experimental Design

351 The assimilation system was run from May 1, 2009 to Dec 31, 2015. Two forward
352 simulations with the prior and posterior fluxes were also conducted from May 1, 2009
353 to Dec 31, 2015, respectively. For both assimilation and forward runs, the initial field
354 of 3-D CO₂ concentrations at 00:00 UTC May 1, 2009 was from the product of CT2017
355 as well, and the MOZART-4 model was run with the resolution of 2.8°×2.8°. The first
356 8 months are considered as a spin-up run, and the results from Jan 1, 2010 to Dec 31,
357 2015 are analyzed and evaluated in this study.

358 During the assimilation, the resolution of λ is the same as the transport model. The



359 BIO CO₂ exchanges and OCN fluxes are optimized in this study, and the FOSSIL and
360 FIRE carbon emissions are kept intact. Following Wang et al., (2019), global annual
361 uncertainties of 100% and 40% are assigned to BIO and OCN CO₂ exchanges,
362 respectively. Accordingly, the uncertainties of the scaling factor (λ) for the prior BIO
363 and OCN fluxes in each DA window at the grid cell level are assigned to 3 and 5,
364 respectively. The model-data mismatch error of XCO₂ is constructed using the GOSAT
365 retrieval error, which is provided along with the ACOS product. According to the
366 previous works of Wang et al. (2019) and Deng et al. (2014), all retrieval errors are also
367 uniformly inflated by a factor of 1.9 in this study, which is the same as Wang et al.
368 (2019), but a lowest error is added in this study, which is fixed as 1 ppm.

369 **4. Results and Discussions**

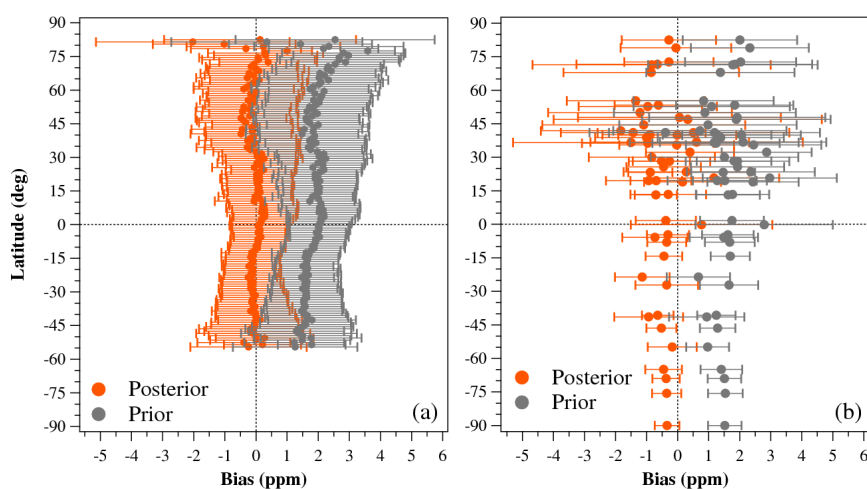
370 **4.1 Evaluation for the inversion results**

371 **4.1.1 Evaluation using Assimilated GOSAT XCO₂ retrievals**

372 Figure 3a shows the zonal mean XCO₂ model-data mismatch errors at different
373 latitudes during the study period. Compared with the GOSAT XCO₂ retrievals, basically
374 all the zonal mean BIAS of the prior XCO₂ in different latitudes are greater than 1 ppm,
375 with a global mean of 1.8 ± 1.3 ppm (average \pm standard deviation, same thereafter), but
376 for the posterior XCO₂, most zonal average BIAS are within ± 0.5 ppm, with global
377 mean of -0.0 ± 1.1 ppm. The global mean RMSE between the simulated and GOSAT
378 retrieved XCO₂ concentrations also decreases from a prior value of 2.2 ppm to 1.1 ppm
379 (Table 1), indicating that the model-data mismatch errors between the simulated and
380 retrieved XCO₂ are significantly reduced. Overall, for both prior and posterior
381 concentrations, the BIAS in the southern hemisphere is smaller than that in the northern
382 hemisphere. In the same hemisphere, the BIAS at low latitudes is smaller than that at
383 high latitudes. Figure 4 shows the spatial distribution of the posterior XCO₂ biases. It
384 could be found that in most grids ($\sim 80\%$), the biases are within ± 1 ppm. In Tropical
385 Pacific, North Pacific, North Atlantic and Tropical Land, most biases are positive, and



386 in the northern extra-tropical lands, negative biases are dominant. This pattern may be
 387 related to the retrieval errors, and the large BIAS in the high latitudes may be attributed
 388 to the large retrieval errors in those areas, which are caused by the lower solar elevation
 389 angle. Overall, this small posterior BIAS, which is less than the retrieval error (Crisp et
 390 al., 2012), indicates that the GCAS system works well with the GOSAT XCO₂ retrievals
 391 in this study.



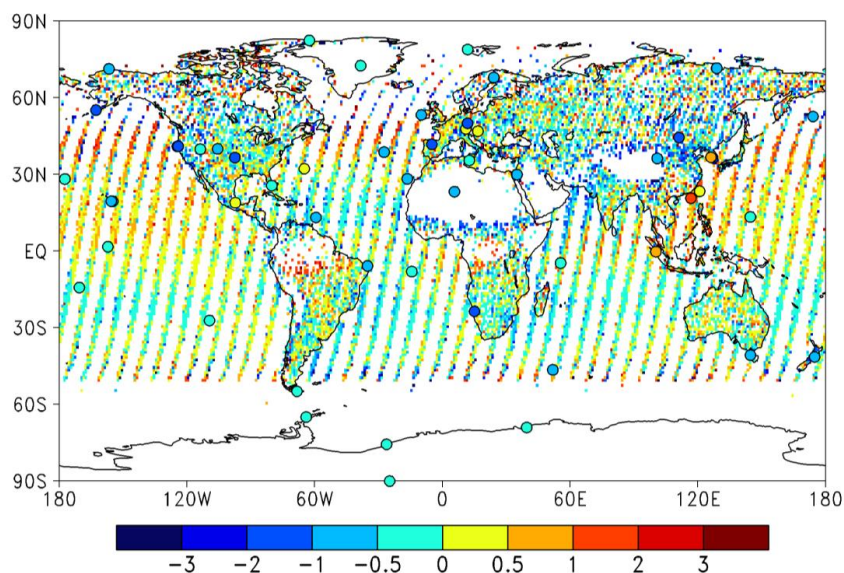
392
 393 **Figure 3.** Biases at different latitudes (a, simulated and retrieved XCO₂; b, simulated
 394 and observed CO₂ mixing ratios; error bar represents the standard deviations of the
 395 biases at each latitude and each site, respectively)

396
 397 **Table 1.** Statistics of the simulated surface CO₂ and XCO₂ concentrations against the
 398 surface flask observations and GOSAT retrievals, respectively

| | BIAS (ppm)* | | RMSE (ppm) | | CORR | |
|-------------------------|-------------|-----------|------------|-----------|-------|-----------|
| | Prior | Posterior | Prior | Posterior | Prior | Posterior |
| XCO ₂ | 1.8±1.3 | -0.0±1.1 | 2.2 | 1.1 | 0.95 | 0.96 |
| Surface CO ₂ | 1.6±1.8 | -0.5±1.8 | 2.4 | 1.9 | 0.96 | 0.96 |

399 *mean ± standard deviation

400



401

402

403

Figure 4. Distributions of the mean biases of the posterior (cycle) surface CO₂ and (grid shaded) XCO₂ concentrations (simulations minus observations/retrievals)

404

4.1.2 Evaluation using independent surface observations

405

406

407

408

409

410

411

412

413

414

415

416

417

418

Figure 3b shows the mean biases of the simulated surface CO₂ mixing ratios at each flask site at different latitudes. It could be found that the BIAS of the prior CO₂ mixing ratios are basically greater than 1 ppm at different latitudes, with global mean of 1.6±1.8 ppm, after constraining using the GOSAT XCO₂ retrievals, the BIAS at most sites are within ±1 ppm, with a global mean of -0.5±1.8 ppm. These BIAS are similar to those of Basu et al. (2013), in which the average model–observation bias decreased from a prior value of 1.95 ppm to -0.55 ppm. In our study, the RMSE between the simulated and surface flask concentrations are also reduced in most sites, with the global mean RMSE decreasing from 2.4 to 1.9 ppm (Table 1). The BIAS in the northern hemisphere are significantly larger than those in southern hemisphere, because the carbon flux in the northern hemisphere is more complex than that of the southern hemisphere (Wang et al., 2019). In addition, the posterior BIAS in most sites are negative, especially in the middle latitudes in the northern hemisphere. The significant negative biases (less than 1 ppm) are mainly distributed in North America, Europe, central Asia, while positive



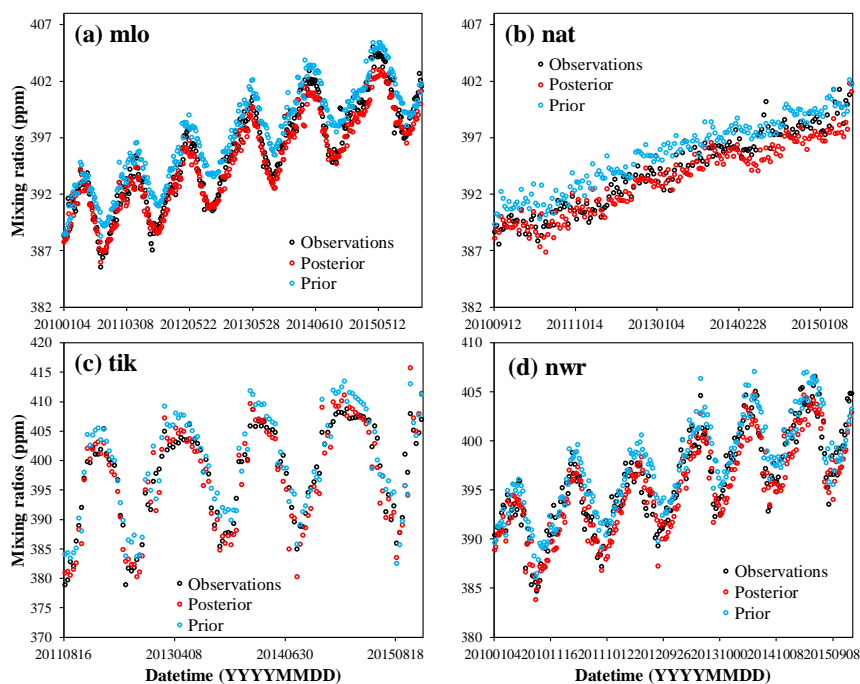
419 biases are mainly located along east Asian coast (Figure 4), indicating that the carbon
420 sinks in North America and Europe might be overestimated in this study, while those in
421 the upwind areas of east Asian coastal sites, mainly eastern China, may be
422 underestimated.

423 Moreover, it also could be found that the global mean prior BIAS of XCO₂ (about
424 1.82 ppm) is greater than the surface concentrations (1.60 ppm), while the BIAS of
425 XCO₂ reduced by inversion (about 1.8 ppm) is less than the reduction of BIAS in the
426 surface concentrations (about 2.1 ppm). This may be attributed to the fact that, on the
427 one hand, although the GOSAT XCO₂ retrievals were bias-corrected, there may still be
428 some systematic deviations; on the other hand, the responses of surface observations to
429 changes in the surface carbon flux is faster than the XCO₂ concentrations, so that larger
430 flux adjustments are needed to match XCO₂ concentration with ground data. A similar
431 situation was reported in Wang et al. (2019). In their study, GOSAT XCO₂ retrievals
432 were used to optimize the terrestrial carbon flux in 2015. Their inversion reduced the
433 BIAS of simulated surface and XCO₂ (compared against TCCON sites) concentrations
434 by about 1.1 and 0.9 ppm, respectively.

435 Figure 5 shows the time series of simulated and observed CO₂ mixing ratios at four
436 sites, i.e., mlo, nwr, tik, and nat. The mlo and nwr sites are two mountain stations located
437 in the center of Pacific and western US, respectively, and nat and tik are two coastal
438 sites located in Amazon and Siberia, respectively (Figure 2). Overall, the posterior
439 mixing ratios have a better agreement with the observations at all 4 sites. The mlo site
440 is an atmospheric baseline station. At mlo, the posterior mixing ratio well reproduces
441 the observed concentration, while the prior concentrations are overestimated all the
442 time since the summer of 2010, especially during the summertime every year. Besides,
443 the posterior concentrations during the wintertime are underestimated, and the
444 underestimation gradually increases along with time. A similar situation also could be
445 found at the nat site as well as other sites located in tropical and southern hemisphere
446 oceans (Figure not shown). Figure S1 shows the interannual variations of the global
447 mean BIAS. Clearly, the biases of surface CO₂ are gradually accumulated, leading to



448 the relatively large mean bias (-0.5 ppm). If we remove the impact of accumulation, the
449 annual bias is about -0.1 ppm per year (about -0.2 PgC yr⁻¹). There are no error
450 accumulations at most land sites like nwr and tik. These indicate that the global net
451 carbon sinks are slightly overestimated every year, but in different lands, there are
452 interannual variations.



453

454

Figure 5. Modeled and observed CO₂ time series at four surface stations

455 **4.2 Global Carbon Budget**

456 Table 2 presents the mean prior and posterior global carbon budgets during 2010 ~
457 2015 of this study. For comparison, the mean global carbon budgets from Global
458 Carbon Budget 2018 (GCP2018, Le Quéré et al., 2018), CT2017, and Jena CarboScope
459 (JCS, Rödenbeck, 2005) are also shown. Both CT2017 and JCS estimates of the
460 surface-atmosphere CO₂ exchange were based on the atmospheric measurements of
461 CO₂ concentrations. In this study, the JCS product of s04oc_v4.3 is adopted. It should
462 to be noted that JCS only provides the land-atmosphere carbon flux, which is the sum



463 of BIO carbon flux and FIRE carbon emissions, and no individual FIRE carbon
464 emissions data is available. To compare, the FIRE carbon emissions used in this study,
465 which is from CT2017, is also applied to the JCS data, namely the BIO carbon flux of
466 JCS in this manuscript is obtained from the land-atmosphere carbon flux of JCS minus
467 the FIRE carbon emission of this study.

468 **Table 2.** Mean global carbon budgets during 2010 ~2015 estimated in this study as well
469 as those from the prior fluxes, GCP2018, CT2017 and JCS (PgC yr⁻¹)

| | Prior | Posterior | GCP2018 | CT2017 | JCS |
|-----------------------------------|-------|-----------|---------|--------|-------|
| Fossil fuel and industry (FOSSIL) | 9.58 | 9.58 | 9.49 | 9.62 | 9.31 |
| Biomass burning (FIRE) | 2.02 | 2.02 | 1.52* | 2.03 | 2.02 |
| Terrestrial ecosystem (BIO) | -4.07 | -4.24 | -3.13 | -4.29 | -4.07 |
| Ocean (OCN) | -2.47 | -2.56 | -2.46 | -2.57 | -2.25 |
| Budget imbalance | - | - | -0.52 | - | - |
| Net biosphere exchange*** | -2.05 | -2.22 | -2.12 | -2.27 | -2.05 |
| Global net carbon flux (AGR) | 5.06 | 4.80 | 4.91** | 4.79 | 5.01 |

470 * land-use change emissions, **atmospheric growth in GCP2018, *** for GCP2018, it
471 is the sum of BIO, FIRE and budget imbalance, and for the others, it is the sum of BIO
472 flux and FIRE emission.

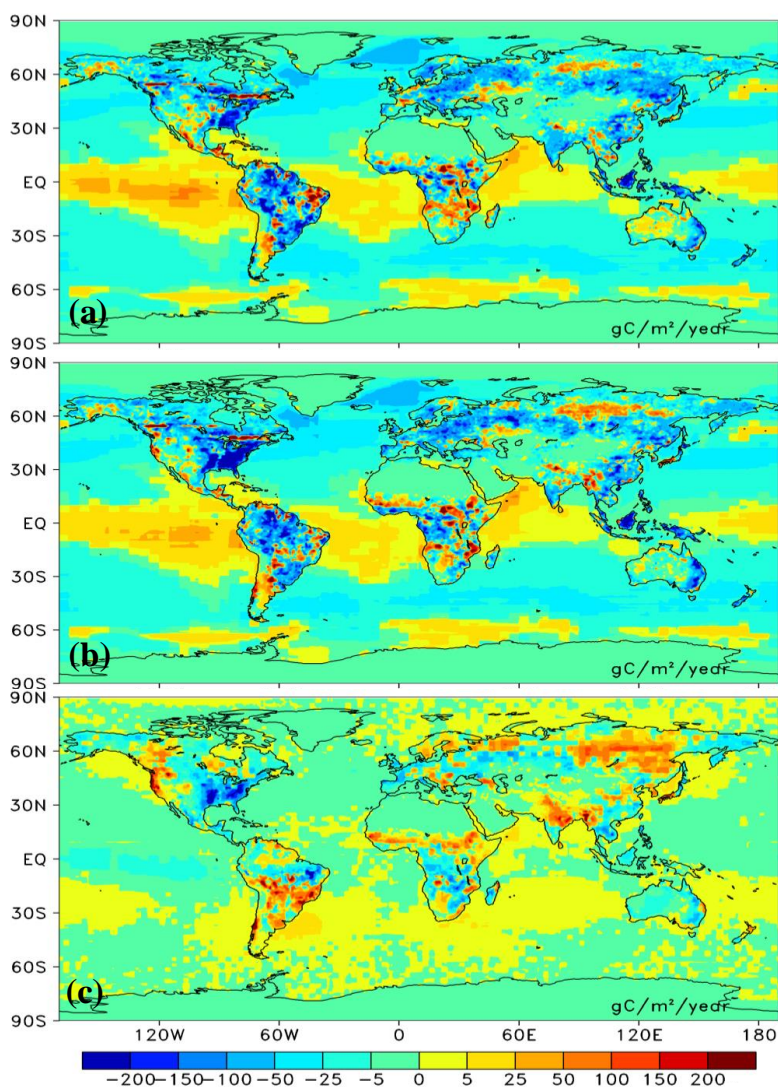
473 The mean posterior BIO carbon flux during 2010-2015 in this study is -4.24 PgC
474 yr⁻¹ (negative/positive mean carbon uptake/release from/to the atmosphere, same
475 thereafter), and the OCN flux is -2.56 PgC yr⁻¹, after considering the FOSSIL carbon
476 emission (9.58 PgC yr⁻¹) and FIRE carbon emission (2.02 PgC yr⁻¹), the mean global
477 net carbon flux (i.e., atmospheric CO₂ growth rate) inverted in this study is 4.80 PgC
478 yr⁻¹. Both the posterior BIO and OCN carbon fluxes are stronger than the prior ones,
479 and the posterior global net carbon flux is weaker than the prior one. Compared with
480 the others, both posterior BIO and OCN fluxes are close to the ones of CT2017, but
481 higher than the ones of JCS. The atmospheric CO₂ growth rate (AGR) of GCP2018 was
482 estimated directly from atmospheric CO₂ measurements, which were provided by the
483 US National Oceanic and Atmospheric Administration Earth System Research
484 Laboratory (NOAA/ESRL) (Dlugokencky and Tans, 2018), and therefore, it could be
485 considered as a true value. The posterior AGR in this study (4.8 PgC yr⁻¹) is slightly



486 lower than GCP2018 and very close to CT2017. Compared with GCP2018, the
487 deviations of prior and JCS AGR are 0.15 and 0.10 PgC yr⁻¹, while the ones of posterior
488 and CT2017 are -0.11 and -0.12 PgC yr⁻¹, respectively.

489 **4.3 Regional Carbon Flux**

490 Figure 6 shows the distributions of the mean prior and posterior annual BIO and
491 OCN carbon fluxes as well as their differences during 2010 - 2015. For the prior BIO
492 flux, carbon uptakes mainly occur over eastern North America, Amazon, southern
493 Brazil, western Europe, southern Russia, eastern China, South Asia and Malay
494 Archipelago; and carbon releases mainly occur in western North America, eastern
495 Amazon, Argentina, most Africa, Indo-China Peninsula, and parts of eastern Europe
496 and Russia. For the prior OCN flux, carbon uptakes mainly happen in mid-latitude
497 regions in both hemispheres, while carbon sources are mainly in tropical oceans and
498 Southern Ocean. After the constraint with the GOSAT XCO₂ retrievals, the overall
499 patterns of carbon sinks and sources are similar to the prior ones. However, the BIO
500 sinks in East and Central America, eastern Amazon, tropical Africa, Indo-China
501 Peninsula, and southwestern Russia are obviously increased, on the contrary, in western
502 North America, temperate South America, extra-tropical Africa, South Asia, Southwest
503 China, North China, Siberia, and parts of southern and northern Europe, the carbon
504 sources are increased. For the OCN flux, in most tropical and northern hemisphere
505 oceans, the carbon sinks are slightly increased, while in most southern hemisphere
506 oceans, the carbon sources are slightly enhanced.



507

508 **Figure 6.** Distributions of mean annual terrestrial ecosystem and ocean carbon fluxes

509 a) prior and b) posterior and c) their differences (posterior - prior) ($\text{gC m}^{-2}\text{yr}^{-1}$)

510 Table 3 lists the aggregated mean annual prior and posterior BIO carbon fluxes
511 during 2010-2015 for the 11 TRANSCOM land regions (Figure 2, Gurney et al., 2002)
512 as well as 3 aggregated large-scale regions, i.e., Northern Lands, Tropical Lands, and
513 Southern Lands. Northern lands include Boreal North America, Temperate North
514 America, Boreal Asia, Temperate Asia and Europe; Tropical Lands include Tropical



515 South America, Tropical Asia, Northern Africa and Southern Africa; and Southern
516 Lands include Temperate South America and Australia. For the prior, there is a largest
517 carbon sink in Tropical South America, followed by Boreal Asia and Temperate Asia,
518 and a weakest carbon flux in Southern Africa. After optimization using GOSAT XCO₂
519 retrievals, the carbon sinks of Temperate North America, Southern Africa are
520 significantly increased, and those in Australia and Europe are also enhanced. However,
521 in Temperate South America, Northern Africa, Boreal Asia, and Temperate Asia, the
522 carbon sinks are decreased. Very small changes are found in Boreal North America,
523 Tropical South America, and Tropical Asia, especially for Tropical South America,
524 however, as shown in Figure 6, there are obvious changes over different areas in
525 Tropical South America, thus the zero change in statistics in this region may be just a
526 coincidence. For the Amazon region (Figure 2), the estimated BIO flux is decreased
527 from a prior of -0.52 PgC yr⁻¹ to -0.45 PgC yr⁻¹. The largest carbon sink occurs in
528 Temperate North America, followed by Tropical South America and Europe, and the
529 weakest sink appears in Northern Africa.

530 For comparisons, Table 3 also lists the mean BIO carbon fluxes of CT2017 and
531 JCS for the same period. For the 3 large-scale regions, i.e., Northern Lands, Tropical
532 Lands and Southern Lands, the same as the global total BIO carbon sink, the carbon
533 sinks in these 3 regions are also similar to CT2017. However, in each region, the
534 distributions of carbon sinks between this study and CT2017 are significantly different.
535 In Northern Lands, the carbon sinks estimated by this study are more evenly distributed,
536 although Temperate North America has the largest carbon sink, and those in Boreal Asia,
537 Temperate Asia and Europe are also very strong and comparable. However, in CT2017,
538 the carbon sinks are mainly distributed in Boreal Asia and Temperate Asia, accounting
539 for more than 70% of the total sink in Northern Lands. The sinks in Temperate North
540 America and Europe are very weak or even neutral. In Tropical Lands, this study shows
541 strong carbon sinks in Tropical South America and Tropical Asia, and a weak sink in
542 Africa, while CT2017 shows an opposite pattern. In Southern Lands, this study shows
543 comparable sinks in Temperate South America and Australia, while CT2017 shows a



544 strong sink in Temperate South America and very weak one in Australia. Compared
 545 with JCS, except for Temperate North America and Southern Africa, the carbon sinks
 546 are comparable in other regions. Constraining with different observations might be one
 547 of the main reasons among these studies. Many studies have shown differences between
 548 the constraints with in situ observations and XCO₂ retrievals (e.g., Wang et al., 2019;
 549 Deng et al., 2014). Besides, these differences may be also related to the different prior
 550 BIO carbon fluxes among these studies, especially for the tropical land. The distribution
 551 of the posterior BIO fluxes in this study and CT2017 are consistent with the
 552 corresponding prior fluxes in the tropical land (Table 3). Using the same GOSAT XCO₂
 553 retrievals, Deng et al. (2014) adopted a similar prior flux with this study, which was
 554 also simulated using the BEPS model but globally neutralized, to infer the land fluxes
 555 of 2010, their distributions are roughly consistent with this study, while Wang et al.
 556 (2019) applied the prior flux from CT2016 to optimizing the fluxes in 2015, and they
 557 showed a similar distribution of land sinks over tropical lands to that of CT2017.

558 **Table 3.** Regional BIO and FIRE flux in the 11 TRANSCOM land regions (PgC yr⁻¹)

| Regions | Fire | This Study | | CT2017 | | JCS |
|-------------------------|-------|------------|-----------|--------|-----------|-------|
| | | Prior | Posterior | Prior | Posterior | |
| Boreal North America | 0.065 | -0.26 | -0.28 | -0.05 | -0.39 | -0.31 |
| Temperate North America | 0.022 | -0.49 | -0.88 | -0.14 | -0.23 | -0.21 |
| Tropical South America | 0.220 | -0.66 | -0.66 | 0.02 | -0.11 | -0.43 |
| Temperate South America | 0.142 | -0.3 | -0.15 | -0.16 | -0.42 | 0.13 |
| Northern Africa | 0.385 | -0.18 | -0.05 | -0.47 | -0.82 | -0.11 |
| Southern Africa | 0.628 | 0.01 | -0.14 | -0.63 | -0.55 | -0.66 |
| Boreal Asia | 0.097 | -0.61 | -0.45 | -0.18 | -0.99 | -0.51 |
| Temperate Asia | 0.065 | -0.51 | -0.42 | -0.15 | -0.66 | -0.69 |
| Tropical Asia | 0.258 | -0.45 | -0.47 | -0.05 | -0.07 | -0.73 |
| Australia | 0.097 | -0.16 | -0.23 | -0.15 | -0.07 | -0.08 |
| Europe | 0.015 | -0.46 | -0.52 | -0.18 | 0 | -0.44 |
| Northern Lands* | 0.26 | -2.33 | -2.55 | -0.7 | -2.27 | -2.16 |
| Tropical Lands** | 1.49 | -1.28 | -1.32 | -1.13 | -1.55 | -1.93 |
| Southern Lands*** | 0.24 | -0.46 | -0.38 | -0.31 | -0.49 | 0.05 |

559 *Northern lands include Boreal North America, Temperate North America, Boreal Asia, Temperate
 560 Asia and Europe; **Tropical Lands include Tropical South America, Tropical Asia, Northern Africa
 561 and Southern Africa; ***Southern Lands include Temperate South America and Australia.



562 Compared with other studies, the land fluxes (including FIRE but excluding
563 FOSSIL) in South America ($-0.45 \text{ PgC yr}^{-1}$), Europe ($-0.51 \text{ PgC yr}^{-1}$), Boreal Asia ($-$
564 0.35 PgC yr^{-1}), Temperate Asia ($-0.35 \text{ PgC yr}^{-1}$), Tropical Asia ($-0.21 \text{ PgC yr}^{-1}$), and
565 Australia ($-0.13 \text{ PgC yr}^{-1}$) are comparable with the forest sinks in these regions during
566 2000-2007 estimated using forest inventory data by Pan et al. (2011). However, the land
567 fluxes in Africa and North America are significantly different from the estimates of Pan
568 et al. (2011). In North America, based on inventory-based calculations, the Second State
569 of the Carbon Cycle Report (SOCCR2, Hayes et al., 2018) estimated that the average
570 annual net land ecosystem flux was $-0.96 \text{ PgC yr}^{-1}$, and after considering the outgassing
571 and wood products emissions, they reported the land-based carbon sink was -0.606 PgC
572 yr^{-1} ($\pm 75\%$) during the 2004 to 2013 time period. The land flux estimated in this study
573 ($-1.07 \text{ PgC yr}^{-1}$) is close to the bottom-up estimate of the net land ecosystem flux, but
574 much stronger than the reported land-based carbon sink of SOCCR2. In Africa, Ciais
575 et al. (2011) shown a comprehensive estimate for its carbon balance, given a sink of $-$
576 0.2 PgC yr^{-1} (excluding land-use change emissions) based upon observations. Our
577 estimate of the BIO flux in Africa is very consistent with this result. Moreover, most
578 recently, Palmer et al. (2019) inferred the carbon fluxes of pan-tropical lands in 2015
579 and 2016 using both GOSAT and the NASA Orbiting Carbon Observatory (OCO-2)
580 XCO_2 retrievals, and their estimated net carbon emissions from African biosphere
581 dominate pan-tropical atmospheric CO_2 signals are similar to the results of this study.
582 In Boreal Asia, the land sink estimated by bottom-up approaches was in the range of $-$
583 $0.11 \sim -0.76 \text{ PgC yr}^{-1}$ (Hayes et al., 2011; Nilsson et al., 2003; Dolman et al., 2012;
584 Zamolodchikov et al., 2017). CarbonTracker usually reports a very stronger carbon sink
585 (Jacobson et al. 2020; Peter et al., 2007; Zhang et al., 2014), one possible reason is that
586 there are no enough surface observations in Asia boreal regions. Saeki et al. (2013b)
587 conducted an inversion with a focus on the Siberia region, and also derived a large sink
588 of $-0.56 \pm 0.79 \text{ PgC yr}^{-1}$ only using the NOAA data, but after adding additional
589 observations in Siberia, they obtained a weaker uptake of $-0.35 \pm 0.61 \text{ PgC yr}^{-1}$. Our
590 estimate ($-0.35 \text{ PgC yr}^{-1}$) is in the range of bottom-up estimates, and very consistent

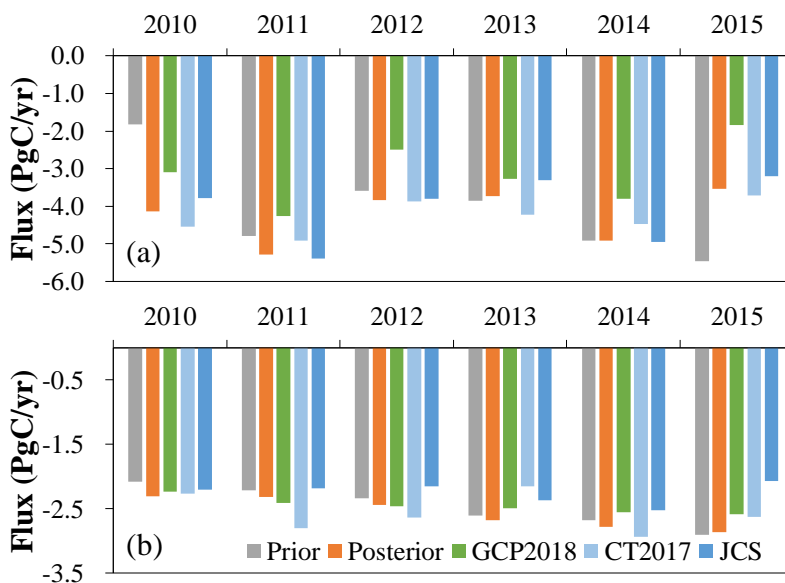


591 with the Siberia-focused inversion (Saeki et al., 2013b). In Europe, previous GOSAT-
592 based inversions consistently derived a very large European sink, which was in the
593 range of $-0.6 \sim -1.8 \text{ PgC yr}^{-1}$ (Basu et al., 2013, Chevallier et al., 2014; Deng et al.,
594 2014), while the ones constrained using surface observations were much weak, in the
595 range of $0 \sim -0.4 \text{ PgC yr}^{-1}$ (Peters et al., 2007, 2010; Peylin et al., 2013; Scholze et al.,
596 2019). Our estimate of the BIO flux in Europe is smaller than the previous GOSAT-
597 based inversions, and close to the estimate of Peylin et al. (2013). In the Amazon region,
598 the posterior land flux is $-0.45 \text{ PgC yr}^{-1}$, which is in the range of the previous long-term
599 forest biomass sink estimates of $-0.28 \sim -0.49 \text{ PgC yr}^{-1}$ (Phillips et al., 2009; Brienen et
600 al., 2015), but larger than the other inversions (e.g., Deng et al., 2016; Gatti et al., 2014).

601 **4.4 Interannual variations**

602 **4.4.1 Global land and ocean fluxes**

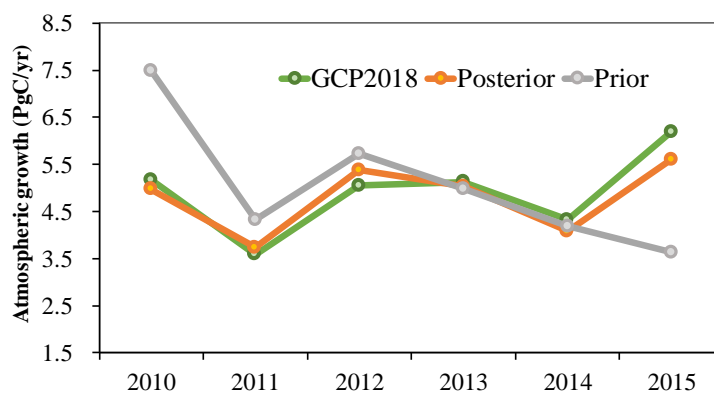
603 Figure 7 shows the interannual variations of the prior and posterior BIO and OCN
604 fluxes. Overall, from 2010 to 2015, the prior BIO fluxes show an increasing trend, but
605 for the posterior fluxes, there is no significant trend. Large differences between the prior
606 and the posterior fluxes mainly occur in 2010 and 2015. In 2010, the posterior sink is
607 much stronger than the prior, while in 2015, the posterior sink is much weaker than the
608 prior. For the OCN flux, both prior and posterior fluxes show consistently upward
609 trends, and except for 2015, the posterior sinks are basically stronger than the prior ones
610 every year. For the AGR (Figure 8), the prior sink shows a significant downward trend,
611 while the posterior one shows a slightly increasing trend. The same as the BIO fluxes,
612 large differences mainly occur in 2010 and 2015.



613

614 **Figure 7.** Interannual variations of global (a) BIO and (b) OCN fluxes of the prior and
615 posterior as well as GCP2018, CarbonTracker 2017 (CT2017) and Jena CarboScope
616 (JCS)

617 Compared with the other products, the interannual variations of the posterior BIO
618 fluxes (Figure 7a) are consistent with the inversions of CT2017 and JCS, and the
619 estimates of GCP2018. For each year, the inversions of this study are all in the range of
620 CT2017 and JCS, but higher than GCP2018. However, because GCP2018 has the item
621 of budget imbalance and the land-use change emission is different from the FIRE
622 emission, the BIO flux in GCP2018 is different from this study, so direct comparison
623 with GCP2018 is not meaningful. For OCN fluxes, overall, there are no significant
624 differences among different estimates, and the upward trend of this study is similar to
625 that of GCP2018, and higher than those of CT2017 and JCS. The interannual variation
626 of AGR in this study is also very consistent with GCP2018 (Figure 8). Except for 2012
627 and 2015, the absolute deviations of AGR between this study and GCP2018 are within
628 0.3 PgC yr^{-1} .

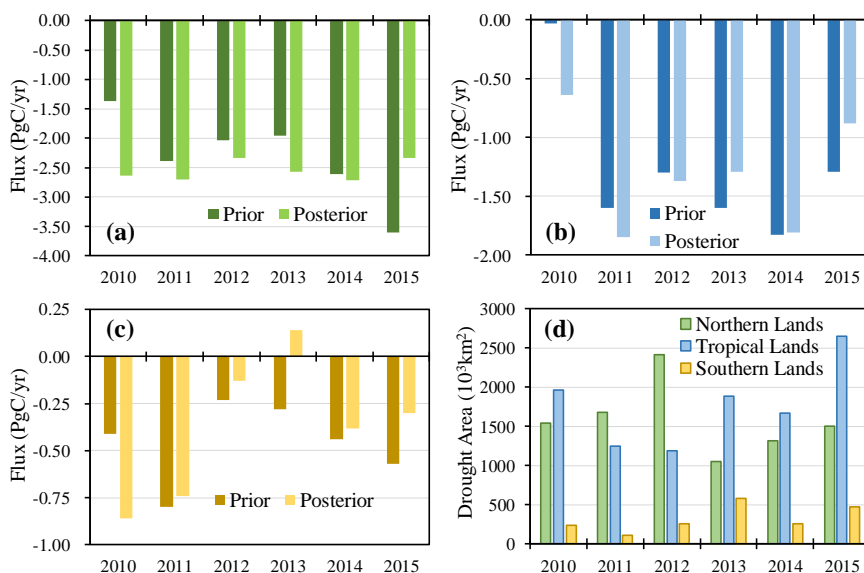


629
630

Figure 8. Interannual variations of the atmospheric CO₂ growth rates

631 4.4.2 Regional land fluxes

632 Figure 9a, b, and c show the prior and posterior interannual variations of the BIO
633 fluxes in Northern Lands, Tropical Lands and Southern Lands, respectively. In Northern
634 Lands, the interannual variations of both prior and posterior fluxes are similar to the
635 corresponding global land totals (Figure 7a), i.e., upward trend for the prior flux and no
636 trend with the posterior one, indicating that the interannual variations of global BIO
637 fluxes are dominated by the fluxes in Northern Lands. In Tropical Lands, the
638 interannual variations of posterior fluxes are similar to the prior ones, however,
639 compared with the prior sinks in 2010 and 2011, the posterior sinks are much stronger,
640 while in 2013 and 2015, they are much weaker. In Southern Lands, there are large
641 differences for the interannual variations between the prior and posterior fluxes. For the
642 prior flux, the highest sink is in 2011 and the weakest in 2012, and after that, it increases
643 year by year, while for the posterior flux, the sink decreases from 2010 to 2013, and
644 then increases.



645

646 **Figure 9.** Prior and posterior interannual variations of the BIO fluxes in (a) Northern
647 Lands, (b) Tropical Lands, and (c) Southern Lands, respectively, and (d) severe
648 drought areas of above 3 regions.

649 Drought is one of the most important factors that affect terrestrial carbon sinks, and
650 generally, severe drought will significantly reduce carbon sinks (e.g., Ma et al., 2012;
651 Zhao and Running, 2010; Ciais et al., 2005; Gatti et al., 2014; Phillips et al., 2009;
652 Vicente-Serrano et al., 2013). Previous studies (e.g., Liu et al., 2018) have used the
653 GOSAT XCO₂ retrievals to infer the impact of droughts on terrestrial ecosystem carbon
654 uptake anomalies. Figure 9d shows the severe drought areas (SDAs) in the 3 large
655 regions every year, which were calculated according to the monthly Standardised
656 Precipitation-Evapotranspiration Index at 12-month time scales (SPEI12) (Beguería et
657 al., 2010). Here, the database of SPEIbase v2.5 is used, and the severe drought is
658 defined as SPEI12 less than -1.5 (Paulo et al., 2012). In addition, only the severe
659 drought that happens in forests, shrubs and crops are counted in this study. It could be
660 found that the posterior fluxes have better correlations with the SDAs in all 3 regions,
661 i.e. a larger SDA leads to a weaker carbon sink, and vice versa. The correlation
662 coefficients between carbon sinks and SDAs in Northern Lands, Tropical Lands and



663 Southern Lands increase from prior values of -0.1, -0.25 and -0.44 to -0.53, -0.67 and -
664 0.76, respectively, indicating that the inversion has improved the interannual variations
665 of BIO fluxes in large scales. In addition, strong El Niño event happened during
666 2015~2016, and many researches have studied the responses of tropical land carbon
667 fluxes to this strong El Niño event (e.g., Wang et al., 2018; Liu et al., 2017; Bastos et
668 al., 2018; Koren et al., 2018). Liu et al. (2017) found that relative to the 2011 La Niña,
669 the pantropical biosphere released 2.5 ± 0.34 PgC more carbon into the atmosphere in
670 2015. Bastos et al. (2018) showed a smaller difference of carbon fluxes between 2015
671 and 2011 using both bottom-up and top-down approaches, which was in the range of
672 $-0.7 \sim -1.9$ PgC yr⁻¹. In this study, compared with the prior, our inversion significantly
673 enhances the difference between 2011 and 2015 (Figure 9b), and shows that 2015
674 released 1.35 PgC more than 2011 in the pantropical region (defined as Liu et al., 2017),
675 which is much smaller than Liu et al.'s result, but agree well with the result of Bastos
676 et al. (2018).

677 Moreover, Figure 10 shows the prior and posterior interannual variations of the
678 BIO fluxes on the 11 TRANSCOM land regions. In North America, including
679 Temperate North America and Boreal North America, the prior fluxes show an upward
680 trend, while the posterior fluxes show a downward trend. In Boreal Asia and Temperate
681 Asia, there are significant upward trends for the prior fluxes, but no significant trends
682 are found in the posterior fluxes. In Temperate South America, although the prior and
683 posterior fluxes show trends of weakening first and then increasing, the years in which
684 the carbon sink is weakest are not consistent: the prior flux is weakest in 2012, while
685 the posterior one is in 2013. Similarly, in northern Africa, the prior and posterior fluxes
686 show a trend of increasing and then decreasing, but the prior flux is the largest in 2014,
687 while the posterior one is strongest in 2011. In other regions, i.e., Tropical South
688 America, Tropical Asia, Southern Africa, Australia and Europe, the trends between the
689 prior and posterior fluxes are similar, especially in Tropical South America and Tropical
690 Asia, the prior and posterior fluxes are very close every year. Among them, in Southern
691 Africa and Australia, the posterior fluxes have more significant interannual variations



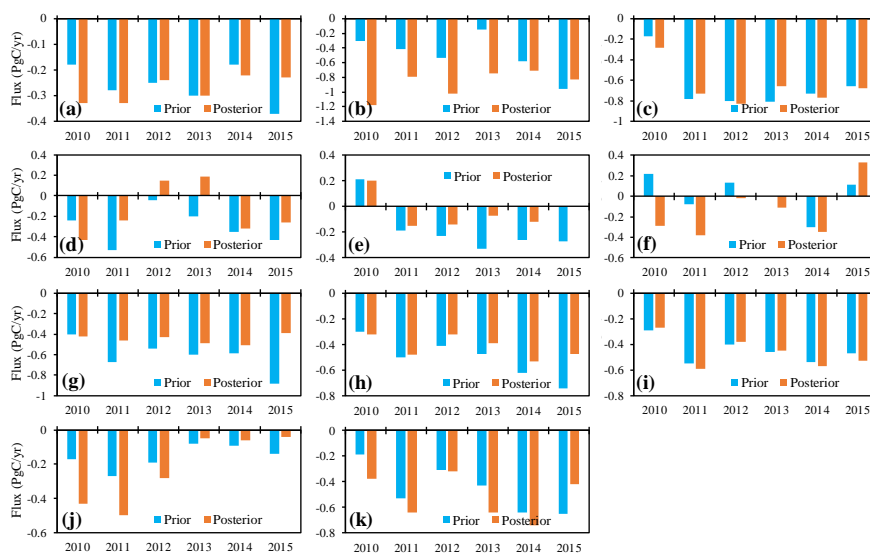
692 than the prior fluxes, and in Europe, the posterior sink is much weaker in 2015, and
693 stronger in 2010 and 2013 than the prior one.

694 The same as above, we also investigate the relationships between the interannual
695 variations of carbon sinks and SDAs in the 11 TRANSCOM land regions. As shown in
696 Table 4, in Temperate South America, Boreal Asia, and Europe, the posterior sinks have
697 a better correlation with the SDAs than the prior sinks, especially in Europe, the
698 correlation coefficient increases from a prior value of -0.33 to -0.85. However, in other
699 regions, there is no obvious improvement, and in some regions, the relationships are
700 even getting worse, such as Boreal North America, Temperate North America, Northern
701 Africa and Southern Africa. One possible reason is that there are usually higher annual
702 mean temperatures in drought years, which might extend the growing season of
703 vegetation, thereby enhance the carbon uptake and offset the impacts of drought. A
704 previous study (Wolf et al., 2016) showed that in 2012, Temperate North America
705 experienced an extreme summer drought event, and along with the warmest spring on
706 record. They quantified the impact of this climate anomaly on the carbon cycle and
707 concluded that the warm spring largely increased spring carbon uptake, and thus
708 compensated for reduced carbon uptake induced by the summer drought. Liu et al.
709 (2018) reported that because of the compensating effect of the carbon flux anomalies
710 between northern and southern US in 2011 and between spring and summer in 2012,
711 the annual carbon uptake decreased by 0.10 ± 0.16 PgC in 2011, and increased by
712 0.10 ± 0.16 GtC in 2012 over US compared with the averaged state. In this study,
713 compared with the mean flux during 2010-2015, the carbon sink in Temperate North
714 America decreased by 0.09 PgC yr⁻¹ in 2011, and increased by 0.14 PgC yr⁻¹ in 2012,
715 which is very close to the result of Liu et al. (2018). In Australia, both the prior and
716 posterior fluxes have very good relationships with the SDAs. The significantly
717 enhanced carbon uptake during 2010-2012 is consistent with the finding in Detmers et
718 al. (2015), who inferred an even stronger carbon sink of -0.77 ± 0.10 PgC yr⁻¹ from the
719 end of 2010 to early 2012 using the GOSAT XCO₂ product, and they confirmed that
720 this enhanced sink is related to the strong La Niña episode, which brought a record-



721 breaking amount of precipitation, resulting in an enhanced growth of vegetation. In
722 Tropical South America, the impacts of the 2010 drought on the carbon uptake over
723 Amazon have been extensively studied (e.g., Doughty et al., 2015; Gatti et al., 2014;
724 van der Laan-Luijkx et al., 2015). 2010 is a drought year, while 2011 is a wet year in
725 the Amazon region, compared to 2011, Gatti et al. (2014) estimated the no-fire carbon
726 exchange was reduced by 0.22 PgC yr^{-1} , van der Laan-Luijkx et al. (2015) derived a
727 decrease of biospheric uptake ranging from 0.08 to 0.26 PgC yr^{-1} , and Doughty et al.
728 (2015) concluded that drought suppressed Amazon-wide photosynthesis by 0.23 – 0.53
729 PgC yr^{-1} . In this study, our inversion reduces the difference of carbon uptake between
730 2010 and 2011 from a prior of 0.62 PgC yr^{-1} to 0.28 PgC yr^{-1} , which is much more
731 consistent with the previous estimates.

732 Carbon uptake occurs mainly through photosynthesis of vegetation leaves. Leaf
733 area index (LAI) is a measure of leaf area per unit area. Buchmann and Schulze (1999)
734 shown that there are strong relationships between the interannual changes of carbon
735 uptake and LAI in grasslands, C4 crops, and coniferous forests, but no significant
736 relationship in broad-leaved forests; Chen et al. (2019) also showed that from 1981 to
737 2016, the increase in LAI contributed significantly to the increase in global BIO carbon
738 sinks. Therefore, we further investigate the relationships between the interannual
739 changes of carbon sinks and LAIs in the 11 TRANSCOM regions (Table 4). Here, the
740 LAI data are from the GIMMS LAI3g product, which has a spatial resolution of $1/12$
741 degree and a time interval of 15 days (Zhu et al., 2013). As shown in Table 4, in Boreal
742 North America, Temperate North America, Northern Africa and Southern Africa,
743 compared with the prior fluxes, there are better relationships between the posterior
744 carbon sinks and LAIs, the correlation coefficients increase from prior values of -0.4 ,
745 0.31 and 0.35 to 0.62 , 0.73 and 0.90 respectively, suggesting that the inversion of this
746 study may also improve the interannual variations of carbon sinks in these 4 regions at
747 a certain extent.



748

749 **Figure 10.** Prior and posterior interannual variations of the BIO fluxes on (a) Boreal
 750 North America, (b) Temperate North America, (c) Tropical South America, (d)
 751 Temperate South America, (e) Northern Africa, (f) Southern Africa, (g) Boreal Asia,
 752 (h) Temperate Asia, (i) Tropical Asia, (j) Australia, and (k) Europe

753

754 **Table 4.** Correlation coefficients of severe drought areas (SDAs) and regional mean
 755 LAI with the BIO sinks in each region

| Regions | SDA | | LAI | |
|-------------------------|-------|-----------|-------|-----------|
| | Prior | Posterior | Prior | Posterior |
| Boreal North America | -0.29 | 0.36 | -0.4 | 0.62 |
| Temperate North America | -0.54 | -0.27 | 0.31 | 0.73 |
| Tropical South America | -0.1 | -0.2 | 0.64 | 0.49 |
| Temperate South America | -0.41 | -0.74 | 0.72 | 0.24 |
| Northern Africa | 0.51 | 0.2 | 0.81 | 0.89 |
| Southern Africa | -0.53 | 0.41 | 0.35 | 0.9 |
| Boreal Asia | -0.17 | -0.35 | 0.49 | 0.1 |
| Temperate Asia | 0.33 | 0.33 | 0.55 | 0.38 |
| Tropical Asia | -0.03 | 0.16 | 0.69 | 0.71 |
| Australia | -0.85 | -0.73 | 0.88 | 0.83 |
| Europe | -0.33 | -0.85 | 0.85 | 0.58 |

756

757



758 **5. Summary and Conclusions**

759 In this study, we upgrade the GCAS system to GCASv2 with new assimilation
760 algorithms, procedures and a localization scheme, a higher assimilation parameter
761 resolution, and the ability to assimilate XCO₂ retrievals. Then, we use the GOSAT
762 XCO₂ retrievals to constrain terrestrial ecosystem and ocean carbon fluxes from May
763 1, 2009 to Dec 31, 2015, using the GCASv2 system. We compare the simulated prior
764 and posterior XCO₂ against the corresponding GOSAT XCO₂ retrievals to test the
765 effectiveness of the assimilation system and evaluate the posterior carbon fluxes by
766 comparing the posterior CO₂ mixing ratios against observations from 52 surface flask
767 sites. The distribution and interannual variations of the posterior carbon fluxes at both
768 global and regional scales from 2010 to 2015 are shown and discussed.

769 Compared with the GOSAT XCO₂ retrievals, the global mean BIAS and RMSE
770 decrease from prior values of 1.8±1.3 and 2.2 ppm to -0.0±1.1 and 1.1 ppm, respectively,
771 indicating that the GCASv2 system works well with the GOSAT XCO₂ retrievals.
772 Independent evaluations using surface flask CO₂ concentrations showed that the
773 posterior carbon fluxes could significantly improve the modeling of atmospheric CO₂
774 concentrations, with the global mean BIAS and RMSE decreasing from prior values of
775 1.6±1.8 and 2.4 ppm to -0.5±1.8 and 1.9 ppm, respectively. The large negative biases
776 are mainly distributed in North America, Europe, indicating the overestimates of carbon
777 sinks over these areas. Evaluations also show that the biases gradually increase along
778 with the time in most tropical and southern hemisphere ocean sites, but no accumulation
779 is found at most land sites, indicating that globally, the carbon sinks may be
780 overestimated every year, but in different lands, the deviations of the estimates may
781 differ each year.

782 Globally, the mean annual BIO carbon sink and the interannual variations
783 inferred in this study are very close to the estimates of CT2017 during the study period,
784 and the estimated mean AGR and interannual changes are also very close to the
785 observations, with mean annual bias of -0.11 PgC yr⁻¹. Regionally, the inversion shows



786 that in the northern lands, the carbon sink of Temperate North America is the strongest,
787 and those in Boreal Asia, Temperate Asia and Europe are also very strong and
788 comparable; in the tropics, there are strong sinks in Tropical South America and
789 Tropical Asia, but a very weak sink in Africa. These distributions are significantly
790 different from the estimates of CT2017, probably due to the different prior fluxes and
791 CO₂ observations used for inversion. However, our estimates in most regions or
792 continents are comparable or in the range of previous bottom-up estimates. The
793 inversion also changed the interannual variations of carbon sinks in most TRANSCOM
794 and hemisphere scale land regions, leading to their better relationship with the
795 variations of severe drought or LAI, indicating that the inversion with GOSAT XCO₂
796 retrievals may help to better understand the interannual variations of regional carbon
797 fluxes.

798

799 **Data availability**

800 The code of GCASv2 system and the inversion results of this study are available to the
801 community and can be accessed upon request from Fei Jiang (jiangf@nju.edu.cn) at
802 Nanjing University.

803 **Author contributions**

804 FJ, JC and WJ designed the research; FJ run the model, analyzed the results and wrote
805 the paper; HW handled the GOSAT XCO₂ retrievals; WH analyzed the drought data;
806 XL run the BEPS model; FJ lead the update of the GCAS system, and XT, HW, JW, SF,
807 GL, ZC, SZ, JL, WH, and MW participated in it; RL, PS and PK provided the surface
808 CO₂ observations; JC, WJ and HW participated in the discussion of the inversion results
809 and provided input on the paper for revision before submission.

810 **Competing interests**

811 The authors declare that they have no conflict of interest.



812 **Acknowledgements**

813 This work is supported by the National Key R&D Program of China (Grant No:
814 2016YFA0600204). We acknowledge all atmospheric data providers to
815 obspack_co2_1_GLOBALVIEWplus_v5.0_2019_08_12. We especially thank Pieter
816 Tans, Ed Dlugokencky, Kenneth Schuldt at NOAA ESRL, USA and Ray Langenfelds,
817 Paul Steele, Paul Krummel at CSIRO, Australia for their great efforts on CO₂
818 observations and data distributions. CarbonTracker CT2017 results are provided by
819 NOAA ESRL, Boulder, Colorado, USA, from the website at
820 <http://carbontracker.noaa.gov>. The GOSAT data are produced by the OCO project at the
821 Jet Propulsion Laboratory, California Institute of Technology, and obtained from the
822 data archive at the NASA Goddard Earth Science Data and Information Services Center.
823 We are also grateful to the High-Performance Computing Center (HPCC) of Nanjing
824 University for doing the numerical calculations in this paper on its blade cluster system.
825

826 **Reference**

- 827 Andres, R. J., Gregg, J. S., Losey, L., Marland, G. and Boden, T. A.: Monthly, global emissions
828 of carbon dioxide from fossil fuel consumption. *Tellus B*, 63(3), 309–327,
829 <https://doi.org/10.1111/j.1600-0889.2011.00530.x>, 2011.
- 830 Archer, C. L., and Jacobson, M. Z.: Evaluation of global wind power, *J. Geophys. Res.*, 110,
831 D12110, <https://doi.org/10.1029/2004JD005462>, 2005.
- 832 Bastos, A., Friedlingstein, P., Sitch, S., Chen, C., Mialon, A., Wigneron, J.-P., Arora, V. K.,
833 Briggs, P. R., Canadell, J. G., and Ciais, P.: Impact of the 2015/2016 El Niño on the
834 terrestrial carbon cycle constrained by bottom-up and top-down approaches. *Philosophical
835 Transactions of the Royal Society B: Biological Sciences*, 373(1760), 20170304,
836 <https://doi.org/10.1098/rstb.2017.0304>, 2018.
- 837 Basu, S., Guerlet, S., Butz, A., Houweling, S., Hasekamp, O., Aben, I., Krummel, P., Steele, P.,
838 Langenfelds, R., Torn, M., Biraud, S., Stephens, B., Andrews, A., and Worthy, D.: Global
839 CO₂ fluxes estimated from GOSAT retrievals of total column CO₂, *Atmos. Chem. Phys.*, 13,
840 8695–8717, <https://doi.org/10.5194/acp-13-8695-2013>, 2013.
- 841 Beguería, S., Vicente-Serrano, S. M., and Angulo-Martinez, M.: A Multiscalar Global Drought
842 Dataset: The SPEIbase: A New Gridded Product for the Analysis of Drought Variability and
843 Impacts. *Bulletin of The American Meteorological Society - BULL AMER METEOROL
844 SOC*, 91, <https://doi.org/10.1175/2010BAMS2988.1>, 2010.



- 845 Brienen, R. J. W., Phillips, O. L., Feldpausch, T. R., Gloor, E., Baker, T. R., Lloyd, J., Lopez-
846 Gonzalez, G., Monteagudo-Mendoza, A., Malhi, Y., Lewis, S. L., Martinez, R. V., Alexiades,
847 M., Davila, E. A., Alvarez-Loayza, P., Andrade, A., Aragao, L., Araujo-Murakami, A., Arets,
848 E., Arroyo, L., Aymard, G. A., Banki, O. S., Baraloto, C., Barroso, J., Bonal, D., Boot, R.
849 G. A., Camargo, J. L. C., Castilho, C. V., Chama, V., Chao, K. J., Chave, J., Comiskey, J.
850 A., Valverde, F. C., da Costa, L., de Oliveira, E. A., Di Fiore, A., Erwin, T. L., Fauset, S.,
851 Forsthofer, M., Galbraith, D. R., Grahame, E. S., Groot, N., Herault, B., Higuchi, N.,
852 Coronado, E. N. H., Keeling, H., Killeen, T. J., Laurance, W. F., Laurance, S., Licona, J.,
853 Magnussen, W. E., Marimon, B. S., Marimon, B. H., Mendoza, C., Neill, D. A., Nogueira,
854 E. M., Nunez, P., Camacho, N. C. P., Parada, A., Pardo-Molina, G., Peacock, J., Pena-Claros,
855 M., Pickavance, G. C., Pitman, N. C. A., Poorter, L., Prieto, A., Quesada, C. A., Ramirez,
856 F., Ramirez-Angulo, H., Restrepo, Z., Roopsind, A., Rudas, A., Salomao, R. P., Schwarz,
857 M., Silva, N., Silva-Espejo, J. E., Silveira, M., Stropp, J., Talbot, J., ter Steege, H., Teran-
858 Aguilar, J., Terborgh, J., Thomas-Caesar, R., Toledo, M., Torello-Raventos, M., Umetzu, R.
859 K., Van der Heijden, G. M. F., Van der Hout, P., Vieira, I. C. G., Vieira, S. A., Vilanova, E.,
860 Vos, V. A., and Zagt, R. J.: Long-term decline of the Amazon carbon sink. *Nature*, 519, 344–
861 348, <https://doi.org/10.1038/nature14283>, 2015.
- 862 Buchmann, N., and Schulze, E.D.: Net CO₂ and H₂O fluxes of terrestrial ecosystems, *Global*
863 *Biogeochem. Cycles*, 13(3), 751–760, <https://doi.org/10.1029/1999GB900016>, 1999.
- 864 Buitenhuis, E., Le Quéré, C., Aumont, O., Beaugrand, G., Bunker, A., Hirst, A., Ikeda, T.,
865 O'Brien, T., Piontkovski, S., and Straile, D.: Biogeochemical fluxes through
866 mesozooplankton, *Global Biogeochem. Cycles*, 20, GB2003,
867 <https://doi.org/10.1029/2005GB002511>, 2006.
- 868 Botta, A., Ramankutty, N., and Foley, J. A.: LBA-ECO LC-04 IBIS model simulations for the
869 Amazon and Tocantins Basins: 1921–1998, ORNL DAAC, Oak Ridge, Tennessee, USA,
870 <https://doi.org/10.3334/ORNLDAAC/1139>, 2012.
- 871 Chen, J. M., Ju, W., Ciais, P., Viovy, N., Liu, R. G., Liu, Y., Lu, X. H.: Vegetation structural
872 change since 1981 significantly enhanced the terrestrial carbon sink. *Nat. Commun.*, 10,
873 4259, <https://doi.org/10.1038/s41467-019-12257-8>, 2019.
- 874 Chen, J. M., Ju, W., Cihlar, J., Price, D., Liu, J., Chen, W., Pan, J., Black, A. and Barr, A.: Spatial
875 distribution of carbon sources and sinks in Canada's forests. *Tellus B*, 55, 622–642,
876 <https://doi.org/10.1034/j.1600-0889.2003.00036.x>, 2003.
- 877 Chen, J. M., Liu, J., Cihlar, J., and Goulden, M. L.: Daily canopy photosynthesis model through
878 temporal and spatial scaling for remote sensing applications, *Ecol. Modell.*, 124, 99–119,
879 [https://doi.org/10.1016/S0304-3800\(99\)00156-8](https://doi.org/10.1016/S0304-3800(99)00156-8), 1999.
- 880 Chen, J. M., Menges, C.H., and Leblanc, S.G.: Global mapping of foliage clumping index using
881 multi-angular satellite data, *Remote Sens. Environ.*, 97 (4), 447–457,
882 <https://doi.org/10.1016/j.rse.2005.05.003>, 2005.
- 883 Chevallier, F., Breon, F.-M., and Rayner, P. J.: Contribution of the Orbiting Carbon Observatory
884 to the estimation of CO₂ sources and sinks: Theoretical study in a variational data



- 885 assimilation framework, *J. Geophys. Res.-Atmos.*, 112, d09307,
886 <https://doi.org/10.1029/2006JD007375>, 2007.
- 887 Chevallier, F., Palmer, P. I., Feng, L., Boesch, H., O'Dell, C. W., and Bousquet, P.: Toward
888 robust and consistent regional CO₂ flux estimates from in situ and spaceborne
889 measurements of atmospheric CO₂, *Geophys. Res. Lett.*, 41, 1065–1070,
890 <https://doi.org/10.1002/2013GL058772>, 2014.
- 891 Ciais, P., Reichstein, M., Viovy, N., Granier, A., Ogee, J., Allard, V., Aubinet, M., Buchmann,
892 N., Bernhofer, C., Carrara, A., Chevallier, F., De Noblet, N., Friend, A. D., Friedlingstein,
893 P., Grunwald, T., Heinesch, B., Keronen, P., Knohl, A., Krinner, G., Loustau, D., Manca, G.,
894 Matteucci, G., Miglietta, F., Ourcival, J. M., Papale, D., Pilegaard, K., Rambal, S., Seufert,
895 G., Soussana, J. F., Sanz, M. J., Schulze, E. D., Vesala, T., and Valentini, R.: Europe-wide
896 reduction in primary productivity caused by the heat and drought in 2003, *Nature*, 437, 529–
897 533, <https://doi.org/10.1038/nature03972>, 2005.
- 898 Ciais, P., Bombelli, A., Williams, M., Piao, S.L., Chave, J., Ryan, C.M., Henry, M., Brender, P.,
899 and Valentini, R.: The carbon balance of Africa: synthesis of recent research studies, *Phil.*
900 *Trans. Roy. Soc. Lond. Math. Phys. Eng. Sci.*, 369, 2038-2057,
901 <https://doi.org/10.1098/rsta.2010.0328>, 2011.
- 902 Crisp, D., Fisher, B., O'Dell, C., Frankenberg, C., Basilio, R., Bosch, H., Brown, L. R., Castano,
903 R., Connor, B., Deutscher, N. M., Eldering, A., Griffith, D., Gunson, M., Kuze, A.,
904 Mandrake, L., McDuffie, J., Messerschmidt, J., Miller, C. E., Morino, I., Natraj, V., Notholt,
905 J., O'Brien, D. M., Oyafuso, F., Polonsky, I., Robinson, J., Salawitch, R., Sherlock, V.,
906 Smyth, M., Suto, H., Taylor, T. E., Thompson, D. R., Wennberg, P. O., Wunch, D. and Yung,
907 Y. L.: The ACOS CO₂ retrieval algorithm - Part II: Global XCO₂ data characterization.
908 *Atmospheric Measurement Techniques*, 5 (4), 687-707, [https://doi.org/10.5194/amt-5-687-](https://doi.org/10.5194/amt-5-687-2012)
909 2012, 2012.
- 910 Deng, F., Jones, D. B. A., Henze, D. K., Bousserrez, N., Bowman, K. W., Fisher, J. B., Nassar,
911 R., O'Dell, C., Wunch, D., Wennberg, P. O., Kort, E. A., Wofsy, S. C., Blumenstock, T.,
912 Deutscher, N. M., Griffith, D. W. T., Hase, F., Heikkinen, P., Sherlock, V., Strong, K.,
913 Sussmann, R., and Warneke, T.: Inferring regional sources and sinks of atmospheric CO₂
914 from GOSAT XCO₂ data, *Atmos. Chem. Phys.*, 14, 3703-3727, [https://doi.org/10.5194/acp-](https://doi.org/10.5194/acp-14-3703-2014)
915 14-3703-2014, 2014.
- 916 Deng, F., Jones, D. B. A., O'Dell, C. W., Nassar, R., and Parazoo, N. C.: Combining GOSAT
917 XCO₂ observations over land and ocean to improve regional CO₂ flux estimates, *J.*
918 *Geophys. Res. Atmos.*, 121, 1896–1913, <https://doi.org/10.1002/2015JD024157>, 2016.
- 919 Detmers, R. G., Hasekamp, O., Aben, I., Houweling, S., van Leeuwen, T. T., Butz, A., Landgraf,
920 J., Köhler, P., Guanter, L., and Poulter, B.: Anomalous carbon uptake in Australia as seen
921 by GOSAT, *Geophys. Res. Lett.*, 42, 8177–8184, <https://doi.org/10.1002/2015GL065161>,
922 2015.
- 923 Dlugokencky, E. and Tans, P.: Trends in atmospheric carbon dioxide, National Oceanic &
924 Atmospheric Administration, Earth System Research Laboratory (NOAA/ESRL), available



- 925 at <http://www.esrl.noaa.gov/gmd/ccgg/trends/global.html>, 2018.
- 926 Doughty, C. E., Metcalfe, D. B., Girardin, C. A. J., Amezquita, F. F., Cabrera, D. G., Huasco,
927 W. H., Silva-Espejo, J. E., Araujo-Murakami, A., da Costa, M. C., Rocha, W., Feldpausch,
928 T. R., Mendoza, A. L. M., da Costa, A. C. L., Meir, P., Phillips, O. L., and Malhi, Y.: Drought
929 impact on forest carbon dynamics and fluxes in Amazonia, *Nature*, 519, 78–82,
930 <https://doi.org/10.1038/nature14213>, 2015.
- 931 Dolman, A. J., Shvidenko, A., Schepaschenko, D., Ciais, P., Tchepakova, N., Chen, T., van der
932 Molen, M. K., Beileli Marchesini, L., Maximov, T. C., Maksyutov, S., and Schulze, E.-D.:
933 An estimate of the terrestrial carbon budget of Russia using inventory-based, eddy
934 covariance and inversion methods, *Biogeosciences*, 9, 5323–5340,
935 <https://doi.org/10.5194/bg-9-5323-2012>, 2012.
- 936 Emmons, L. K., Walters, S., Hess, P. G., Lamarque, J.-F., Pfister, G. G., Fillmore, D., Granier,
937 C., Guenther, A., Kinnison, D., Laepple, T., Orlando, J., Tie, X., Tyndall, G., Wiedinmyer,
938 C., Baughcum, S. L., and Kloster, S.: Description and evaluation of the Model for Ozone
939 and Related chemical Tracers, version 4 (MOZART-4), *Geosci. Model Dev.*, 3, 43–67,
940 <https://doi.org/10.5194/gmd-3-43-2010>, 2010.
- 941 Enting, I. G., and Newsam, G. N.: Atmospheric constituent inversion problems: Implications
942 for baseline monitoring, *J. Atmos. Chem.*, 11, 69–87, <https://doi.org/10.1007/BF00053668>,
943 1990.
- 944 Feng, S., Jiang, F., Wu, Z., Wang, H., Ju, W., and Wang, H.: CO emissions inferred from surface
945 CO observations over China in December 2013 and 2017. *Journal of Geophysical Research:
946 Atmospheres*, 125, <https://doi.org/10.1029/2019JD031808>, 2020.
- 947 Gatti, L. V., Gloor, M., Miller, J. B., Doughty, C. E., Malhi, Y., Domingues, L. G., Basso, L. S.,
948 Martinewski, A., Correia, C. S. C., Borges, V. F., Freitas, S., Braz, R., Anderson, L. O.,
949 Rocha, H., Grace, J., Phillips, O. L., and Lloyd, J.: Drought sensitivity of Amazonian carbon
950 balance revealed by atmospheric measurements. *Nature* 506, 76–80,
951 <https://doi.org/10.1038/nature12957>, 2014.
- 952 Giglio, L., Randerson, J. T., and van der Werf, G. R.: Analysis of daily, monthly, and annual
953 burned area using the fourth-generation global fire emissions database (GFED4) *J.
954 Geophys. Res. Biogeosci.*, 118, 317–328, <https://doi.org/10.1002/jgrg.20042>, 2013.
- 955 Gurney, K. R., Law, R. M., Denning, A. S., Rayner, P. J., Baker, D., Bousquet, P., Bruhwiler,
956 L., Chen, Y.-H., Ciais, P., Fan, S., Fung, I. Y., Gloor, M., Heimann, M., Higuchi, K., John,
957 J., Maki, T., Maksyutov, S., Masarie, K., Peylin, P., Prather, M., Pak, B. C., Randerson, J.,
958 Sarmiento, J., Taguchi, S., Takahashi, T., and Yuen, C.-W.: Towards robust regional esti-
959 mates of CO₂ sources and sinks using atmospheric transport models, *Nature*, 415, 626–630,
960 <https://doi.org/10.1038/415626a>, 2002.
- 961 Hayes, D. J., Vargas, R., Alin, S. R., Conant, R. T., Hutyra, L. R., Jacobson, A. R., Kurz,
962 W. A., Liu, S., McGuire, A. D., Poulter, B., and Woodall, C. W.: Chapter 2: The
963 North American carbon budget. In *Second State of the Carbon Cycle Report
964 (SOCCR2): A Sustained Assessment Report* [Cavallaro, N., G. Shrestha, R. Birdsey,



- 965 M. A. Mayes, R. G. Najjar, S. C. Reed, P. Romero-Lankao, and Z. Zhu (eds.)). U.S.
966 Global Change Research Program, Washington, DC, USA, pp. 71-108,
967 <https://doi.org/10.7930/SOCCR2.2018.Ch2>, 2018.
- 968 Hayes, D. J., McGuire, A. D., Kicklighter, D. W., Gurney, K. R., Burnside, T. J., and Melillo, J.
969 M.: Is the northern high-latitude land-based CO₂ sink weakening?, *Global Biogeochem.*
970 *Cycles*, 25, GB3018, <https://doi.org/10.1029/2010GB003813>, 2011.
- 971 He, L., Chen, J., Pisek, J., Schaaf, C.B., and Strahler, A.H.: Global clumping index map derived
972 from the MODIS BRDF product, *Remote Sens. Environ.*, 119, 118-130,
973 <https://doi.org/10.1016/j.rse.2011.12.008>, 2012.
- 974 Houtekamer, P. L., and Mitchell, H. L.: A sequential ensemble Kalman filter for atmospheric
975 data assimilation, *Monthly Weather Review*, 129(1), 123-137,
976 [https://doi.org/10.1175/1520-0493\(2001\)129<0123:ASEKFF>2.0.CO;2](https://doi.org/10.1175/1520-0493(2001)129<0123:ASEKFF>2.0.CO;2), 2001.
- 977 Houweling, S., Baker, D., Basu, S., Boesch, H., Butz, A., Chevallier, F., Deng, F., Dlugokencky,
978 E. J., Feng, L., Ganshin, A., Hasekamp, O., Jones, D., Maksyutov, S., Marshall, J., Oda, T.,
979 O'Dell, C. W., Oshchepkov, S., Palmer, P. I., Peylin, P., Poussi, Z., Reum, F., Takagi, H.,
980 Yoshida, Y., and Zhuravlev, R.: An intercomparison of inverse models for estimating
981 sources and sinks of CO₂ using GOSAT measurements, *J. Geophys. Res.-Atmos.*, 120,
982 5253–5266, <https://doi.org/10.1002/2014JD022962>, 2015.
- 983 Hungershofer, K., Breon, F.-M., Peylin, P., Chevallier, F., Rayner, P., Klonecki, A., Houweling,
984 S., and Marshall, J.: Evaluation of various observing systems for the global monitoring of
985 CO₂ surface fluxes, *Atmos. Chem. Phys.*, 10, 10503–10520, <https://doi.org/10.5194/acp-10-10503-2010>, 2010.
- 987 IPCC, 2014: Climate Change 2014: Synthesis Report. Contribution of Working Groups I, II and
988 III to the Fifth Assessment Report of the Intergovernmental Panel on Climate Change [Core
989 Writing Team, R.K. Pachauri and L.A. Meyer (eds.)]. IPCC, Geneva, Switzerland, 151 pp.
- 990 Jacobson, A. R., K. N. Schuldt, J. B. Miller, T. Oda, P. Tans, A. Andrews, J. Mund, L. Ott, G. J.
991 Collatz, T. Aalto, S. Afshar, K. Aikin, S. Aoki, F. Apadula, B. Baier, P. Bergamaschi, A.
992 Beyersdorf, S. C. Biraud, A. Bollenbacher, D. Bowling, G. Brailsford, J. B. Abshire, G.
993 Chen, H. Chen, L. Chmura, Sites Climadat, A. Colomb, S. Conil, A. Cox, P. Cristofanelli,
994 E. Cuevas, R. Curcoll, C. D. Sloop, K. Davis, S. D. Wekker, M. Delmotte, J. P. DiGangi, E.
995 Dlugokencky, J. Ehleringer, J. W. Elkins, L. Emmenegger, M. L. Fischer, G. Forster, A.
996 Frumau, M. Galkowski, L. V. Gatti, E. Gloor, T. Griffis, S. Hammer, L. Haszpra, J.
997 Hatakka, M. Heliasz, A. Hensen, O. Hermanssen, E. Hintsa, J. Holst, D. Jaffe, A. Karion, S.
998 R. Kawa, R. Keeling, P. Keronen, P. Kolari, K. Kominkova, E. Kort, P. Krummel, D.
999 Kubistin, C. Labuschagne, R. Langenfelds, O. Laurent, T. Laurila, T. Lauvaux, B. Law, J.
1000 Lee, I. Lechner, M. Leuenberger, I. Levin, J. Levula, J. Lin, M. Lindauer, Z. Loh, M. Lopez,
1001 C. Lund Myhre, T. Machida, I. Mammarella, G. Manca, A. Manning, A. Manning, M. V.
1002 Marek, P. Marklund, M. Y. Martin, H. Matsueda, K. McKain, H. Meijer, F. Meinhardt,
1003 N. Miles, C. E. Miller, M. Molder, S. Montzka, F. Moore, J.-A. Morgui, S. Morimoto, B.
1004 Munger, J. Necki, S. Newman, S. Nichol, Y. Niwa, S. O'Doherty, M. Ottosson-Lofvenius,
1005 B. Paplawsky, J. Peischl, O. Peltola, J.-M. Pichon, S. Piper, C. Plass-Dolmer, M. Ramonet,



- 1006 E. Reyes-Sanchez, S. Richardson, H. Riris, T. Ryerson, K. Saito, M. Sargent, Y. Sawa, D.
1007 Say, B. Scheeren, M. Schmidt, A. Schmidt, M. Schumacher, P. Shepson, M. Shook, K.
1008 Stanley, M. Steinbacher, B. Stephens, C. Sweeney, K. Thoning, M. Torn, J. Turnbull,
1009 K. Tørseth, P. V. D. Bulk, I. T. V. D. Laan-Luijkx, D. V. Dinther, A. Vermeulen, B. Viner, G.
1010 Vitkova, S. Walker, D. Weyrauch, S. Wofsy, D. Worthy, D. Young, and M. Zimnoch.
1011 CarbonTracker CT2019, <https://doi.org/10.25925/39m3-6069>, 2020.
- 1012 Jiang, F., Wang, H.M., Chen, J.M., Zhou, L.X., Ju, W.M., Ding, A.J., Liu, L.X., and Peters, W.:
1013 Nested atmospheric inversion for the terrestrial carbon sources and sinks in China,
1014 *Biogeosciences*, 10(8), 5311~5324, <https://doi.org/10.5194/bg-10-5311-2013>, 2013.
- 1015 Jiang, F., Chen, J. M., Zhou, L. X., Ju, W. M., Zhang, H. F., Machida T., Ciais, P., Peters, W.,
1016 Wang, H. M., Chen, B. Z., Liu, L. X., Zhang, C. H., Matsueda, H., and Sawa, Y.: A
1017 comprehensive estimate of recent carbon sinks in China using both top-down and bottom-
1018 up approaches, *Scientific Reports*, 6, 22130, <https://doi.org/10.1038/srep22130>, 2016.
- 1019 Jin, J., Lin, H. X., Heemink, A., and Segers, A.: Spatially varying parameter estimation for dust
1020 emissions using reduced-tangent-linearization 4DVar, *Atmospheric Environment*, 187, 358-
1021 373, <https://10.1016/j.atmosenv.2018.05.060>, 2018.
- 1022 Ju, W. M., Chen, J. M., Black T. A., Barr A. G., Liu, J., and Chen, B. Z.: Modelling multi-year
1023 coupled carbon and water fluxes in a boreal aspen forest, *Agr. Forest Meteorol.*, 140, 136-
1024 151, <https://doi.org/10.1016/j.agrformet.2006.08.008>, 2006.
- 1025 Koren, G., Van Schaik, E., Araújo, A.C., Boersma, K.F., Gärtner, A., Killaars, L., Kooreman,
1026 M.L., Kruijt, B., Van der Laan-Luijkx, I.T., Von Randow, C., Smith, N.E., and Peters, W.:
1027 Widespread reduction in sun-induced fluorescence from the Amazon during the 2015/2016
1028 El Niño. *Phil. Trans. R. Soc. B*, 373: 20170408. <http://dx.doi.org/10.1098/rstb.2017.0408>,
1029 2018.
- 1030 Kuze, A., Suto, H., Nakajima, M., and Hamazaki, T.: Thermal and near infrared sensor for
1031 carbon observation Fourier-transform spectrometer on the Greenhouse Gases Observing
1032 Satellite for greenhouse gases monitoring, *Appl. Opt.*, 48, 6716, [https://doi.org/10.1364](https://doi.org/10.1364/AO.48.006716)
1033 /AO.48.006716, 2009.
- 1034 Le Quéré, C., R. M. Andrew, P. Friedlingstein, S. Sitch, J. Hauck, J. Pongratz, P. A. Pickers, J.
1035 Ivar Korsbakken, G. P. Peters, J. G. Canadell, A. Arneeth, V. K. Arora, L. Barbero, A. Bastos,
1036 L. Bopp, F. Chevallier, L. P. Chini, P. Ciais, S. C. Doney, T. Gkritzalis, D. S. Goll, I. Harris,
1037 V. Haverd, F. M. Hoffman, M. Hoppema, R. A. Houghton, G. Hurtt, T. Ilyina, A. K. Jain, T.
1038 Johannesen, C. D. Jones, E. Kato, R. F. Keeling, K. K. Goldewijk, P. Landschützer, N.
1039 Lefèvre, S. Lienert, Z. Liu, D. Lombardozi, N. Metz, D. R. Munro, J. E. M. S. Nabel, S.
1040 Nakaoka, C. Neill, A. Olsen, T. Ono, P. Patra, A. Pregon, W. Peters, P. Peylin, B. Pfeil, D.
1041 Pierrot, B. Poulter, G. Rehder, L. Resplandy, E. Robertson, M. Rocher, C. Rödenbeck, U.
1042 Schuster, J. Schwinger, R. Séférian, I. Skjelvan, T. Steinhoff, A. Sutton, P. P. Tans, H. Tian,
1043 B. Tilbrook, F. N. Tubiello, I. T. van der Laan-Luijkx, G. R. van der Werf, N. Viovy, A. P.
1044 Walker, A. J. Wiltshire, R. Wright, S. Zaehle, B. Zheng: Global Carbon Budget 2018, *Earth*
1045 *Syst. Sci. Data*, <https://doi.org/10.5194/essd-10-2141-2018>, 2018.



- 1046 Liu, Y., Liu, R. G., and Chen, J. M.: Retrospective retrieval of long-term consistent global leaf
1047 area index (1981–2011) from combined AVHRR and MODIS data, *J. Geophys. Res.*, 117,
1048 G04003, <https://doi.org/10.1029/2012JG002084>, 2012.
- 1049 Liu, J., Bowman, K., Parazoo, N. C., Bloom, A. A., Wunch, D., Jiang, Z., Gurney, K. R., and
1050 Schimel, D.: Detecting drought impact on terrestrial biosphere carbon fluxes over
1051 contiguous US with satellite observations, *Environmental Research Letters*, 13(9), 095003,
1052 <https://doi.org/10.1088/1748-9326/aad5ef>, 2018.
- 1053 Liu, J., Bowman, K. W., Schimel, D. S., Parazoo, N. C., Jiang, Z., Lee, M., Bloom, A. A.,
1054 Wunch, D., Frankenberg, C., Sun, Y., O'Dell, C. W., Gurney, K. R., Menemenlis, D.,
1055 Gierach, M., Crisp, D., and Eldering, A.: Contrasting carbon cycle responses of the tropical
1056 continents to the 2015–2016 El Niño, *Science*, 358, eaam5690,
1057 <https://doi.org/10.1126/science.aam5690>, 2017.
- 1058 Ma, Z. H., Peng, C. H., Zhu, Q., Chen, H., Yu, G. R., Li, W. Z., Zhou, X. L., Wang, W. F., and
1059 Zhang, W. H.: Regional drought-induced reduction in the biomass carbon sink of Canada's
1060 boreal forests, *Proceedings of the National Academy of Sciences*, 109 (7), 2423-2427;
1061 <https://doi.org/10.1073/pnas.1111576109>, 2012.
- 1062 Maksyutov, S., Takagi, H., Valsala, V. K., Saito, M., Oda, T., Saeki, T., Belikov, D. A., Saito,
1063 R., Ito, A., Yo-shida, Y., Morino, I., Uchino, O., Andres, R. J., and Yokota, T.: Regional CO₂
1064 flux estimates for 2009–2010 based on GOSAT and ground-based CO₂ observations, *Atmos.*
1065 *Chem. Phys.*, 13, 9351–9373, <https://doi.org/10.5194/acp-13-9351-2013>, 2013.
- 1066 Miller, C. E., Crisp, D., DeCola, P. L., Olsen, S. C., Randerson, J. T., Michalak, A. M., Alkhaled,
1067 A., Rayner, P., Jacob, D. J., Suntharalingam, P., Jones, D. B. A., Denning, A. S., Nicholls,
1068 M. E., Doney, S. C., Pawson, S., Boesch, H., Connor, B. J., Fung, I. Y., O'Brien, D.,
1069 Salawitch, R. J., Sander, S. P., Sen, B., Tans, P., Toon, G. C., Wennberg, P. O., Wofsy, S. C.,
1070 Yung, Y. L., and Law, R. M.: Precision requirements for space-based XCO₂ data, *J.*
1071 *Geophys. Res.*, 112, D10314, <https://doi.org/10.1029/2006JD007659>, 2007.
- 1072 Miyazaki, K., Eskes, H. J., Sudo, K., Takigawa, M., van Weele, M., and Boersma, K. F.:
1073 Simultaneous assimilation of satellite NO₂, O₃, CO, and HNO₃ data for the analysis of
1074 tropospheric chemical composition and emissions. *Atmospheric Chemistry and Physics*,
1075 12(20), 9545-9579, <https://doi.org/10.5194/acp-12-9545-2012>, 2012.
- 1076 Nilsson S., Vaganov, E. A., Shvidenko, A., Stolbovoi, V., Rozhkov, V. A., McCallum, I., and
1077 Jonas, M.: Carbon budget of vegetation ecosystems of Russia, *Doklady Earth Sci.*, 363A,
1078 1281–1283, 2003.
- 1079 ObsPack: Cooperative Global Atmospheric Data Integration Project: Multi-laboratory
1080 compilation of atmospheric carbon dioxide data for the period 1957-2018;
1081 [obspace_co2_1_GLOBALVIEWplus_v5.0_2019_08_12](https://doi.org/10.25925/20190812); NOAA Earth System Research
1082 Laboratory, Global Monitoring Division, <http://dx.doi.org/10.25925/20190812>, 2019.
- 1083 Oda, T. and Maksyutov, S.: A very high-resolution (1 km x 1 km) global fossil fuel CO₂
1084 emission inventory derived using a point source database and satellite observations of
1085 nighttime lights. *Atmos. Chem. Phys.* 11, 543–556, <https://doi.org/10.5194/acp-11-543->



- 1086 2011, 2011.
- 1087 O'Dell, C., Connor, B., Bösch, H., O'Brien, D., Frankenberg, C., Castano, R., Christi, M.,
1088 Eldering, D., Fisher, B., Gunson, M., McDuffie, J., Miller, C. E., Natraj, V., Oyafuso, F.,
1089 Polonsky, I., Smyth, M., Taylor, T., Toon, G., Wennberg, P., and Wunch, D.: The ACOS CO₂
1090 retrieval algorithm – Part 1: Description and validation against synthetic observations,
1091 *Atmos. Meas. Tech.*, 5, 99–121, <https://doi.org/10.5194/amt-5-99-2012>, 2012.
- 1092 Palmer, P. I., Feng, L., Baker, D., Chevallier, F., Bösch, H., and Somkuti, P.: Net carbon
1093 emissions from African biosphere dominate pan-tropical atmospheric CO₂ signal, *Nature*
1094 *communications*, 10, 3344, <https://doi.org/10.1038/s41467-019-11097-w>, 2019.
- 1095 Pan, Y., Birdsey, R. A., Fang, J., Houghton, R., Kauppi, P. E., Kurz, W. A., Phillips, O. L.,
1096 Shvidenko, A., Lewis, S. L., Canadell, J. G., Ciais, P., Jackson, R. B., Pacala, S., McGuire,
1097 A. D., Piao, S., Rautiainen, A., Sitch, S., and Hayes, D.: A large and persistent carbon sink
1098 in the world's forests, *Science*, 333, 988–993, <https://doi.org/10.1126/science.1201609>,
1099 2011.
- 1100 Paulo, A. A., Rosa, R. D., and Pereira, L. S.: Climate trends and behavior of drought indices
1101 based on precipitation and evapotranspiration in Portugal, *Nat. Hazards Earth Syst. Sci.*, 12,
1102 1481–1491, <https://doi.org/10.5194/nhess-12-1481-2012>, 2012.
- 1103 Peters, W., Jacobson, A. R., Sweeney, C., Andrews, A. E., Conway, T. J., Masarie, K., Miller, J.
1104 B., Bruh-wiler, L. M. P., P'etron, G., Hirsch, A. I., Worthy, D. E. J., Werf, G. R. V. D.,
1105 Randerson, J. T., Wennberg, P. O., Krol, M. C., and Tans, P. P.: An atmospheric perspective
1106 on North American carbon dioxide exchange: CarbonTracker, *P. Natl. Acad. Sci.*, 104,
1107 18925–18930, <https://doi.org/10.1073/pnas.0708986104>, 2007.
- 1108 Peters, W., Krol, M. C., van der Werf, G. R., Houweling, S., Jones, C. D., Hughes, J., Schaefer,
1109 K., Masarie, K. A., Jacobson, A. R., Miller, J. B., Cho, C. H., Ramonet, M., Schmidt, M.,
1110 Ciattaglia, L., Apadula, F., Helta, D., Meinhardt, F., di Sarra, A. G., Piacentino, S., Sferlazzo,
1111 D., Aalto, T., Hatakka, J., Strom, J., Haszpra, L., Meijer, H. A. J., van der Laan, S., Neubert,
1112 R. E. M., Jordan, A., Rodo, X., Morgui, J. A., Vermeulen, A. T., Popa, E., Rozanski, K.,
1113 Zimnoch, M., Manning, A. C., Leuenberger, M., Uglietti, C., Dolman, A. J., Ciais, P.,
1114 Heimann, M., and Tans, P. P.: Seven years of recent European net terrestrial carbon dioxide
1115 exchange constrained by atmospheric observations, *Glob. Change Biol.*, 16, 1317–1337,
1116 <https://doi.org/10.1111/j.1365-2486.2009.02078.x>, 2010.
- 1117 Peylin, P., Law, R. M., Gurney, K. R., Chevallier, F., Jacobson, A. R., Maki, T., Niwa, Y., Patra,
1118 P. K., Peters, W., Rayner, P. J., Rödenbeck, C., van der Laan-Luijkx, I. T., and Zhang, X.:
1119 Global atmospheric carbon budget: results from an ensemble of atmospheric CO₂ inversions,
1120 *Biogeosciences*, 10, 6699–6720, <https://doi.org/10.5194/bg-10-6699-2013>, 2013.
- 1121 Phillips, O. L., Aragao, L., Lewis, S. L., Fisher, J. B., Lloyd, J., Lopez-Gonzalez, G., Malhi, Y.,
1122 Monteagudo, A., Peacock, J., Quesada, C. A., van der Heijden, G., Almeida, S., Amaral, I.,
1123 Arroyo, L., Aymard, G., Baker, T. R., Banki, O., Blanc, L., Bonal, D., Brando, P., Chave, J.,
1124 de Oliveira, A. C. A., Cardozo, N. D., Czimczik, C. I., Feldpausch, T. R., Freitas, M. A.,
1125 Gloor, E., Higuchi, N., Jimenez, E., Lloyd, G., Meir, P., Mendoza, C., Morel, A., Neill, D.



- 1126 A., Nepstad, D., Patino, S., Penuela, M. C., Prieto, A., Ramirez, F., Schwarz, M., Silva, J.,
1127 Silveira, M., Thomas, A. S., ter Steege, H., Stropp, J., Vasquez, R., Zelazowski, P., Davila,
1128 E. A., Andelman, S., Andrade, A., Chao, K. J., Erwin, T., Di Fiore, A., Honorio, E., Keeling,
1129 H., Killeen, T. J., Laurance, W. F., Cruz, A. P., Pitman, N. C. A., Vargas, P. N., Ramirez-
1130 Angulo, H., Rudas, A., Salamao, R., Silva, N., Terborgh, J., and Torres-Lezama, A.: Drought
1131 sensitivity of the Amazon forest, *Science*, 323, 1344–1347, [https://doi.org/](https://doi.org/10.1126/science.1164033)
1132 [10.1126/science.1164033](https://doi.org/10.1126/science.1164033), 2009.
- 1133 Rödenbeck, C.: Estimating CO₂ sources and sinks from atmospheric mixing ratio
1134 measurements using a global inversion of atmospheric transport, Technical Report 6, Max
1135 Planck Institute for Biogeochemistry, Jena, 2005.
- 1136 Saeki, T., Maksyutov, S., Saito, M., Valsala, V., Oda, T., Andres, R. J., Belikov, D., Tans, P.,
1137 Dlugokencky, E., Yoshida, Y., Morino, I., Uchino, O., and Yokota, T.: Inverse modeling of
1138 CO₂ fluxes using GOSAT data and multi-year ground-based observations, *SOLA*, 9, 45–50,
1139 <https://doi.org/10.2151/sola.2013-011>, 2013a.
- 1140 Saeki, T., Maksyutov, S., Sasakawa, M., Machida, T., Arshinov, M., Tans, P., Conway, T. J.,
1141 Saito, M., Valsala, V., Oda, T., Andres, R. J., and Belikov, D.: Carbon flux estimation for
1142 Siberia by inverse modeling constrained by aircraft and tower CO₂ measurements, *J.*
1143 *Geophys. Res. Atmos.*, 118, 1100–1122, <https://doi.org/10.1002/jgrd.50127>, 2013b.
- 1144 Scholze, M., Kaminski, T., Knorr, W., Voßbeck, M., Wu, M., Ferrazzoli, P., Kerr, Y., Mialon,
1145 A., Richaume P., Rodríguez-Fernández, N., Vittucci, C., Wigneron, J.-P., Mecklenburg, S.,
1146 and Drusch, M.: Mean European carbon sink over 2010–2015 estimated by simultaneous
1147 assimilation of atmospheric CO₂, soil moisture, and vegetation optical depth. *Geophysical*
1148 *Research Letters*, 46, 13796–13803, <https://doi.org/10.1029/2019GL085725>, 2019.
- 1149 Takagi, H., Saeki, T., Oda, T., Saito, M., Valsala, V., Belikov, D., Saito, R., Yoshida, Y., Morino,
1150 I., Uchino, O., Andres, R. J., Yokota, T., and Maksyutov, S.: On the Benefit of GOSAT
1151 Observations to the Estimation of Regional CO₂ Fluxes, *SOLA*, 7, 161–164,
1152 <https://doi.org/10.2151/sola.2011-041>, 2011.
- 1153 Takahashi, T., Sutherland, S. C., Wanninkhof, R., Sweeney, C., Feely, R. A., Chipman, D. W.,
1154 Hales, B., Friederich, G., Chavez, F., Sabine, C., Watson, A., Bakker, D. C. E., Schuster, U.,
1155 Metzl, N., Yoshikawa-Inoue, H., Ishii, M., Midorikawa, T., Nojiri, Y., Körtzinger, A.,
1156 Steinhoff, T., Hoppema, M., Olafsson, J., Arnarson, T. S., Tilbrook, B., Johannessen, T.,
1157 Olsen, A., Bellerby, R., Wong, C.S., Delille, B., Bates, N.R., de Baar, H. J.W.:
1158 Climatological mean and decadal change in surface ocean pCO₂, and net sea-air CO₂ flux
1159 over the global oceans. *Deep Sea Research Part II: Topical Studies in Oceanography*, 56 (8-
1160 10): 554–577, <https://doi.org/10.1016/j.dsr2.2008.12.009>, 2009.
- 1161 van der Laan-Luijkx, I. T., van der Velde, I. R., Krol, M. C., Gatti, L. V., Domingues, L. G.,
1162 Correia, C. S. C., Miller, J. B., Gloor, M., van Leeuwen, T. T., Kaiser, J. W., Wiedinmyer,
1163 C., Basu, S., Clerbaux, C., and Peters, W.: Response of the Amazon carbon balance to the
1164 2010 drought derived with CarbonTracker South America, *Global Biogeochem. Cycles*, 29,
1165 1092–1108, <https://doi.org/10.1002/2014GB005082>, 2015.



- 1166 van der Werf, G. R., Randerson, J. T., Giglio, L., Collatz, G. J., Mu, M., Kasibhatla, P. S.,
1167 Morton, D. C., DeFries, R. S., Jin, Y., and van Leeuwen, T. T.: Global fire emissions and
1168 the contribution of deforestation, savanna, forest, agricultural, and peat fires (1997–2009),
1169 *Atmos. Chem. Phys.*, 10, 11707–11735, <https://doi.org/10.5194/acp-10-11707-2010>, 2010.
- 1170 Vicente-Serrano, S. M., Gouveia, C., Camarero, J. J., Beguería, S., Trigo, R., López-Moreno, J.
1171 I., Azorín-Molina, C., Pasho, E., Lorenzo-Lacruz, J., Revuelto, J., and Morán-Tejeda, E.:
1172 Response of vegetation to drought time-scales across global land biomes, *P. Natl. Acad. Sci.*
1173 *USA.*, 110, 52–57, <https://doi.org/10.1073/pnas.1207068110>, 2013.
- 1174 Wang, H. M., Jiang, F., Wang, J., Ju, W. M., and Chen, J. M.: Terrestrial ecosystem carbon flux
1175 estimated using GOSAT and OCO-2 XCO₂ retrievals, *Atmos. Chem. Phys.*, 19, 12067–
1176 12082, <https://doi.org/10.5194/acp-19-12067-2019>, 2019.
- 1177 Wang, J., Zeng, N., Wang, M. R., Jiang, F., Wang, H. M., Jiang, Z. Q.: Contrasting terrestrial
1178 carbon cycle responses to the 1997/98 and 2015/16 extreme El Niño events, *Earth System*
1179 *Dynamics*, 9, 1–14, <https://doi.org/10.5194/esd-9-1-2018>, 2018.
- 1180 Wang, J. S., Kawa, S. R., Collatz, G. J., Sasakawa, M., Gatti, L. V., Machida, T., Liu, Y., and
1181 Manyin, M. E.: A global synthesis inversion analysis of recent variability in CO₂ fluxes
1182 using GOSAT and in situ observations, *Atmos. Chem. Phys.*, 18, 11097–11124,
1183 <https://doi.org/10.5194/acp-18-11097-2018>, 2018.
- 1184 Whitaker, J. S., and Hamill, T. M.: Ensemble data assimilation without perturbed observations.
1185 *Monthly Weather Review*, 130(7), 1913–1924. [https://doi.org/10.1175/1520-0493\(2002\)130<1913:Edawpo>2.0.Co;2](https://doi.org/10.1175/1520-0493(2002)130<1913:Edawpo>2.0.Co;2), 2002.
- 1187 Wolf, S., Keenan, T. F., Fisher, J. B., Baldocchi, D. D., Desai, A. R., Richardson, A. D., Scott,
1188 R. L., Law, B. E., Litvak, M. E., Brunsell, N. A., Peters, W., and van der Laan-Luijkx, I. T.,
1189 Warm spring reduced carbon cycle impact of the 2012 US summer drought, *Proceedings of*
1190 *the National Academy of Sciences*, 113 (21) 5880–5885;
1191 <https://doi.org/10.1073/pnas.1519620113>, 2016.
- 1192 Wunch, D., Wennberg, P. O., Toon, G. C., Connor, B. J., Fisher, B., Osterman, G. B.,
1193 Frankenberg, C., Man-drake, L., O'Dell, C., Ahonen, P., Biraud, S. C., Castano, R., Cressie,
1194 N., Crisp, D., Deutscher, N. M., Eldering, A., Fisher, M. L., Griffith, D. W. T., Gunson, M.,
1195 Heikkinen, P., Keppel-Aleks, G., Kyrö, E., Lindenmaier, R., Macatangay, R., Mendonca, J.,
1196 Messerschmidt, J., Miller, C. E., Morino, I., Notholt, J., Oyafuso, F. A., Rettinger, M.,
1197 Robinson, J., Roehl, C. M., Salawitch, R. J., Sherlock, V., Strong, K., Sussmann, R., Tanaka,
1198 T., Thompson, D. R., Uchino, O., Warneke, T., and Wofsy, S. C.: A method for evaluating
1199 bias in global measurements of CO₂ total columns from space, *Atmos. Chem. Phys.*, 11,
1200 12317–12337, <https://doi.org/10.5194/acp-11-12317-2011>, 2011.
- 1201 Zamolodchikov, D.G., Grabovskii, V.I., Shulyak, P.P. et al. Recent decrease in carbon sink to
1202 Russian forests. *Dokl Biol Sci* 476, 200–202, <https://doi.org/10.1134/S0012496617050064>,
1203 2017.
- 1204 Zhang, S., Zheng, X., Chen, J. M., Chen, Z., Dan, B., Yi, X., Wang, L., and Wu, G.: A global
1205 carbon assimilation system using a modified ensemble Kalman filter, *Geosci. Model Dev.*,



- 1206 8, 805–816, <https://doi.org/10.5194/gmd-8-805-2015>, 2015.
- 1207 Zhao, M. S., and Running, S. W.: Drought-Induced Reduction in Global Terrestrial Net Primary
1208 Production from 2000 Through 2009, *Science*, 329, 940-943,
1209 <https://doi.org/10.1126/science.1192666>, 2010.
- 1210 Zhang, H. F., Chen, B. Z., van der Laan-Luijk, I. T., Machida, T., Matsueda, H., Sawa, Y.,
1211 Fukuyama, Y., Langenfelds, R., van der Schoot, M., Xu, G., Yan, J. W., Cheng, M. L., Zhou,
1212 L. X., Tans, P. P., and Peters, W.: Estimating Asian terrestrial carbon fluxes from
1213 CONTRAIL aircraft and surface CO₂ observations for the period 2006–2010, *Atmos. Chem.*
1214 *Phys.*, 14, 5807–5824, <https://doi.org/10.5194/acp-14-5807-2014>, 2014.
- 1215 Zhu, Z., Bi, J., Pan, Y., Ganguly, S., Anav, A., Xu, L., Samanta, A., Piao, S., Nemani, R.R., and
1216 Myneni, R. B.: Global Data Sets of Vegetation Leaf Area Index (LAI)_{3g} and Fraction of
1217 Photosynthetically Active Radiation (FPAR)_{3g} Derived from Global Inventory Modeling
1218 and Mapping Studies (GIMMS) Normalized Difference Vegetation Index (NDVI)_{3g} for the
1219 Period 1981 to 2011, *Remote Sensing*, 5, 927-948, <https://doi.org/10.3390/rs5020927>, 2013.
- 1220